On the Nationwide Variability of Low-Level Jets Prior to Warm-season Nocturnal Rainfall in China Revealed by Radar Wind Profilers

Ning Li[a,b,c], Jianping Guo[a,d*], Xiaoran Guo[a,d], Tianmeng Chen[a,d], Zhen Zhang[a], Na Tang[a], Yifei Wang[a], Honglong Yang[d], Yongguang Zheng[c], Yongshui Zhou[e]

[a] *State Key Laboratory of Severe Weather Meteorological Science and Technology & Specialized Meteorological Support Technology Research Center, Chinese Academy of Meteorological Sciences, Beijing 100081, China*

[b] *College of Earth and Planetary Sciences, University of Chinese Academy of Sciences, Beijing 100049, China*

[c] *National Meteorological Centre, Beijing 100081, China*

[d] *CMA Field Scientific Experiment Base for Low-Altitude Economy Meteorological Support of Unmanned Aviation in Guangdong-Hong Kong-Macao Greater Bay Area, Shenzhen 518108, China*

[e] *Guizhou Meteorological Observatory, Guiyang 550001, China*

Correspondence to:

Dr./Prof. Jianping Guo (Email: jpguocams@gmail.com)

Abstract

Nocturnal rainfall initiation is closely linked to low-level jets (LLJs), but national-scale LLJ features over China—especially their evolution preceding warm-season nocturnal rainfall—remain unknown due to scarce high-resolution vertical observations. Here, we reveal the fine vertical structure of LLJs and their rapid evolution within 2 hours preceding the onset of nocturnal heavy rain (HR) and non-HR across four phases of rainy seasons in China during the warm season (April–October) of 2023–2024, utilizing data from a nationwide network of radar wind profilers (RWPs) in combination with surface observations and reanalysis data. Results show that nocturnal rainfall accounted for over 50% of warm-season rainfall, with 56% preceded by LLJs within 2 hours of its onset. In monsoon regions, ~ 45% of nocturnal HR were LLJ-associated (LLJ_HR), producing heavier rainfall than non-LLJ_HR events. Critically, LLJ_HR events underwent a minute-scale 'rapid reorganization' of the LLJ structure, characterized by oscillatory evolution in jet height, frequency and strength. This creates a favorable environment for the 'final-stage intensification' of dynamic field during the last ~30 min, where widespread intensification of jet—coupled with significant thermodynamic instability—act as a primary dynamical forcing mechanism and a key precursor signal for HR initiation. In stark contrast, LLJ_non-HR events exhibited quasi-steady or weakening dynamical trends, accompanied by an inadequate thermodynamic response that lacks such synergistic coupling. These findings demonstrate that minute-scale dynamic adjustments driven by swift evolution of the LLJ are essential for nocturnal HR, offering critical observational constraints for regional model parameterizations and nowcasting accuracy.

Short Summary

Nighttime rainfall often links to low-level jets (LLJs), but we lack clarity on nationwide LLJ features. We here used a nationwide radar wind profiler network to study LLJ changes 2 hours before rainfall, covering China's 2023–2024 rainy seasons. 56% nighttime rainfall had LLJs. The LLJs-associated heavy rain needed a rapid adjustment of LLJs' vertical structure, especially a significant intensification within 30 minutes preceding rain. This shows the importance of LLJ in nowcasting rainfall.

1. Introduction

Forecasting nocturnal heavy rainfall (HR) and associated severe convective weather remains a major challenge in hazardous weather prediction (Davis et al., 2003; Trier et al., 2006), owing to the complexity of triggering mechanisms, the scarcity of continuous high-resolution observations, and inaccuracies in model parameterizations (Carbone and Tuttle, 2008; Reif and Bluestein, 2017; Weckwerth et al., 2019; Zhao et al., 2025). Crucially, the low-level jet (LLJ) that exhibit a diurnal cycle with a maximum at night is widely recognized as a key contributor to nocturnal HR (Bonner 1968; Mitchell et al., 1995; Tuttle and Davis, 2006), as documented in regions or countries such as the Great Plains of the United States (Maddox, 1983; Higgins et al., 1997), Argentina (Marengo et al., 2004), India (Monaghan et al., 2010), North China Plain (Li et al., 2024).

The LLJs primarily originate from the inertial oscillations (IO) following the sudden decay of turbulence after sunset (Blackadar, 1957) and thermal imbalances induced baroclinicity over sloping terrain (Holton, 1967). Functioning as concentrated corridors for heat, moisture, and momentum transport, LLJs can modulate the diurnal oscillation in water vapor by IO (Rasmusson, 1967; Zhang et al., 2019) and enhance convective instability, particularly when elevated high-θ_e air encounters frontal boundaries (Trier et al., 2017). Also, strong low-level vertical wind shear (VWS) associated with LLJs necessarily benefits deep lifting (Maddox et al., 1979; Stensrud, 1996; Rasmussen and Houze, 2016). These mechanisms collectively provide essential thermodynamic and dynamic support for the initiation and organization of nocturnal convection, especially where LLJs force low-level ascent at jet termini or via positive vorticity advection left of the jet axis (Chen et al., 2017; Du and Chen, 2019; Xia and Zhao, 2009).

Furthermore, LLJs interact synergistically with other key factors to trigger HR that is associated with mesoscale convective systems (Chen et al. 2010; Chen et al., 2017; Chen et al., 2024), including terrain effects (Anthes et al., 1982; Pan and Chen, 2019; Huang et al., 2020), gravity waves (Weckwerth & Wakimoto, 1992), among others.

These interactions are highly sensitive to the prevailing synoptic and subsynoptic-scale environmental conditions (e.g., Hodges and Pu, 2019) and fine-scale structural of LLJs, including LLJ frequency, spatial redistribution, and particularly localized wind profile accelerations (Pitchford and London, 1962; Walters and Winkler, 2008; Du and Chen, 2019; Li et al., 2024). Understanding these intricate evolution features of LLJs is critical for improving the forecasting of nocturnal HR.

Despite advances facilitated by regional reanalysis (e.g., Doubler et al., 2015; Li et al., 2021), numerical modeling (e.g., Zhang and Meng, 2019), radiosonde observations (e.g., Whiteman et al., 1997; Yan et al., 2020), and emerging artificial intelligence techniques (e.g., Subrahmanyam et al., 2024) in understanding the climatology and physical mechanisms of LLJs and their role in HR forecasting, significant knowledge gaps remain. The insufficient spatiotemporal resolution of conventional observing systems limits the ability to capture rapid pre-storm environmental changes (Weisman et al., 2015; Cao et al., 2025; Roots et al., 2025), thereby hindering systematic analysis of the fine-scale structure of LLJs and their minute-scale evolution within the critical 2-hour window preceding rainfall.

Moreover, the mechanisms and impacts of LLJs exhibit considerable variation across monsoon phases and geographic regions. As a classic monsoon climate region, China exhibits particularly prominent nocturnal rainfall contributions across major climate-sensitive areas (Yu et al., 2014), where LLJs play a crucial role in modulating primary rainfall belts (Sun, 1986; Chen et al., 2010; Wang et al., 2013; Horinouchi et al., 2019), such as those in Eastern China (Chen et al., 2017; Xue et al., 2018) and South China (Du et al., 2020; Bai et al., 2021; Fu et al., 2021). However, nationwide comparative studies examining LLJ precursor signals across different monsoon phases in China are still lacking.

Radar wind profilers (RWPs) can offer transformative potential by capturing minute-resolution wind profiles to reveal pre-rainfall dynamic precursors (Zamora et al., 1987; Du et al., 2012; Molod et al., 2019; Guo et al., 2023). For example, Gebauer et al. (2018) demonstrated the capability of RWPs to elucidate how heterogeneous structures of LLJ trigger nocturnal convection in Great Plains; Based on a linear net of

RWPs deployed across the North China Plain, our previous study (Li et al., 2024) observed rapid intensification of moisture flux convergence (MFC) driven by a surge in LLJs profile within 30 min preceding nocturnal rainfall onset, highlighting the sensitivity of RWP to minute-scale perturbations of LLJs profiles. However, it remains an open question whether this minute-scale precursor is universally applicable across diverse monsoon phases throughout mainland China. Furthermore, the systematic differences in the fine-scale LLJ evolution that distinguish HR from non-HR have yet to be fully elucidated.

Therefore, this study utilizes a nationwide network of RWPs to address the following two questions: 1) How do the vertical structure of LLJs and their minute-scale evolution within 0–2 hours preceding nocturnal rainfall vary across different rainy season phases? and 2) What are the systematic differences in LLJ dynamic-thermodynamic mechanisms between LLJ-influenced HR and non-HR events? The remainder of this paper is structured as follows: Section 2 details data and methodology, Section 3 presents comparative analyses of characteristics of rainfall and LLJs evolution, and Section 4 synthesizes key conclusions.

2. Data and Methodology

2.1 Radar wind profiler measurements

The RWP observations collected from 31 stations across China (Fig.1) from April to October in 2023–2024 were analyzed in this study, which can provide wind speed and direction with a vertical resolution of 120 m and an interval of 6 minutes (Liu et al., 2019). To reduce the potential influence of poor data quality, RWP data underwent strict quality control following procedures proposed by Wei et al. (2014) and Miao et al. (2018). Firstly, to minimize contamination from precipitation particles, which can introduce significant errors in Doppler-based wind retrieval, all observations during rainfall periods were removed. Secondly, within each profile below 3 km above ground level (AGL), missing values and significant outliers that were defined as values exceeding 2.5 standard deviations from the mean were removed. Next, for each profile, if more than 40% of the data points below 3 km AGL were outliers or missing, that

entire profile was discarded. Finally, discontinuous, or missing data points were estimated using linear interpolation. Following this quality control process, 109,400 wind profiles were discarded and a total of 2,606,042 profiles across China were available for analysis during the study period.

2.2 Multi-source meteorological data

In addition, 1-min rainfall measurements were directly acquired from the rain gauge measurements at 2160 national weather stations across China to identify rainfall events. Rainfall amounts were accumulated over 6-min intervals to ensure temporal alignment with the RWP measurements. Ground-based meteorological variables are measured at 1-min intervals from national weather stations, including 2-m air temperature, relative humidity, and surface pressure. All ground-based data have undergone rigorous quality control (China Meteorological Administration, 2020; Zhao et al., 2024) and are publicly accessible at the National Meteorological Information Center of China Meteorological Administration (CMA).

Furthermore, to diagnose large-scale circulation patterns and environmental conditions preceding nocturnal rainfall influenced by LLJs, this study utilized meteorological variables derived from the fifth generation of the European Centre for Medium-Range Weather Forecasts atmospheric reanalysis (ERA5) of the global climate (Hersbach et al., 2020). The ERA5 data features a horizontal resolution of 0.25°×0.25° across 37 vertical pressure levels and hourly temporal resolution. Unless otherwise specified, all datasets cover the study period of April to October in 2023–2024.

2.3 Identification of nocturnal rainfall events

Firstly, days with typhoon activity were excluded. To minimize the impact of rainfall on RWP measurements, a minimum dry interval of 2 hours was required between consecutive rainfall events. Following the methodology of Li et al. (2024), a rainfall occurrence was defined when the accumulated rainfall measured by all rain gauges within a 25-km radius of each RWP station exceeded 0.1 mm. To account for

rainfall intermittency and filter out transient noise, a valid rainfall event required the initial detection to be followed by at least two subsequent occurrences within 30 min. Any isolated initial occurrence not meeting this criterion was discarded. Notably, this 25-km radius serves as a rigorous spatial constraint to not only mitigates the limitations of single-gauge measurements but also ensures the onset of rainfall at this scale are temporally coherent with that of the rain gauge co-located with RWP (as confirmed by sensitivity tests in Fig. S1 and Table S1). This guarantees direct physical coupling between local rainfall and the RWP-observed wind profiles.

Nocturnal rainfall events were defined as those occurring between 2000 and 0800 Local Standard Time (LST). Based on operational classifications from the National Water Resources Bureau and CMA, the rainy season was categorized into four consecutive phases: (1) the South China Pre-summer Rainy Season (April 1 to June 8, 2023 and April 1 to June 9, 2024), (2) the Meiyu Season (June 9 to July 14, 2023 and June 10 to July 21, 2024), (3) the North China Rainy Season (July 15 to August 31, 2023 and July 22 to August 31, 2024), and (4) the West China Autumn Rainy Season (September 1 to October 31 for both 2023 and 2024). These phases are subsequently designated as Phase 1 to Phase 4 throughout this study. Four regions of interest (ROIs) were subsequently selected for detailed analysis (see Table 1).

Further screening identified locally nocturnal HR events, where the mean 6-min rainfall intensity exceeded the 75th percentile of all recorded rainfall events at each station. This threshold can effectively distinguish significant HR from weak rainfall while ensuring a sufficient sample size for robust statistical analysis of minute-scale LLJ dynamics (Table S1). Furthermore, a sensitivity test by varying the thresholds to 85th and 95th percentile to ensure that the main conclusion regarding the precursory signals of LLJs is robust within a reasonable threshold range (see Figs. S2–S5).

Statistical analysis revealed 3,155 nocturnal rainfall events during the 2023–2024 warm seasons (within the 31 red circles shown in Fig.1). Event counts per rainy season phase were 1,109, 689, 652, and 705 respectively, with 841 events classified as nocturnal HR events.

2.4 Identification of LLJs and associated rainfall event

To ensure identified LLJs exhibit significant vertical wind shear characteristic of jet-like profiles, the following criteria are adopted: (1) a maximum horizontal wind speed exceeding 10 m s^{-1} in the lowest 3 km AGL, and (2) a wind speed reduction of at least 3 m s^{-1} from the maximum to minimum below 3 km AGL, or to 3 km AGL if no minimum exists. These deliberately conservative wind speed thresholds maximize LLJ sample size for enhanced statistical robustness. This definition standard has been widely adopted in previous studies (Bonner, 1968; Whiteman et al., 1997; Du et al., 2014; Yan et al., 2020). The strength of LLJ or jet nose is defined as the maximum wind speed along the entire profile. The LLJ core height is defined as the altitude of the wind speed maximum during LLJ occurrences. Correspondingly, the LLJ direction is determined by the wind direction at the height of the LLJ.

We define rainfall events where LLJ occurs at least twice within 2 hours before rainfall as an LLJ event (Li et al., 2024). The HR events influenced by LLJs (LLJ_HR events), HR events without LLJ influence (non-LLJ_HR events), and non-HR events affected by LLJ (LLJ_non-HR events) are further distinguished.

3. Results and discussion

3.1 General characteristics of nocturnal rainfall and LLJs

Firstly, we characterized the spatiotemporal patterns of rainfall and LLJs observed nationwide during the 2023-2024 warm season. Nationally, nocturnal rainfall accounted for 50.9% of total warm-season rainfall, with pronounced concentrations over North, Northeast and Southwest China (Figs. 2d and 2g). In contrast, the pronounced daytime rainfall dominance in South China (Fig. 2a) may arise from the interaction between enhanced onshore monsoonal flows and terrain (Bai et al., 2020), sea breeze fronts and cold pool (Chen et al., 2016). In terms of frequency, nocturnal rainfall occurred more frequently, constituting 52.5% of the total rainfall frequency versus 47.5% for the daytime, with the highest nocturnal proportions found in southwestern and eastern regions (Figs. 2e and 2h). Although the national mean rainfall

intensity was generally lower at night (1.2 mm/h) than during the day (1.8 mm/h; Figs. 2c and 2f), the probability of nocturnal HR occurrence was significant (51.3%), particularly across western, North, and northeastern China (Fig. 2i).

Figure 3 displays the key attributes of LLJs detected at all 31 RWPs across China using the criteria defined in Section 2. Nocturnal LLJ activity occurred more frequently, with an overall occurrence frequency increase of nearly 18% relative to diurnal LLJs (Figs. 3a and 3e). This pronounced nighttime enhancement is consistent with the classical IO mechanism, whereby reduced surface friction after sunset allows the decoupled boundary layer to accelerate and form stronger LLJs. Spatially, both daytime and nighttime LLJs were more prevalent in eastern and southeastern China, particularly along the Yangtze River basin and coastal regions, where moisture-rich monsoonal flows dominate. In contrast, lower frequencies were observed over northwestern China, likely reflecting weaker large-scale moisture transport and reduced baroclinicity in arid inland regions.

In terms of jet core height (Figs. 3b and 3f), nocturnal LLJs generally exhibited slightly lower core altitudes compared to their daytime counterparts, with most cores concentrated below ~1500 m. This lowering of the jet core at night is consistent with boundary-layer stabilization and the formation of a shallow nocturnal inversion, which confines the jet maximum to lower altitudes. Regarding jet intensity (Figs. 3c and 3g), nighttime LLJs were typically stronger, with a higher proportion of stations reporting wind speeds exceeding 16–18 m s^{-1}. The combination of enhanced wind speed and reduced core height suggests a more concentrated and dynamically organized jet structure during nighttime hours. The dominant wind directions (Figs. 3d and 3h) further reflect regional circulation controls. Southeasterly and southwesterly LLJs prevailed in eastern China, consistent with the transport of warm, moist air from the South China Sea and western Pacific during the warm season. In northern and northwestern regions, LLJs exhibited more variable directional characteristics, likely influenced by synoptic-scale pressure gradients and topographic channeling effects.

Overall, Fig. 3 demonstrates that nocturnal LLJs are not only more frequent but also stronger and lower in altitude than their daytime counterparts. These structural differences imply enhanced moisture transport efficiency and greater potential for nighttime convective organization, providing a dynamical foundation for the observed diurnal asymmetry in heavy rainfall occurrence examined in subsequent sections.

Statistical analysis revealed a substantial linkage between LLJs and nocturnal rainfall. Specifically, 56% of all nocturnal rainfall events across China were preceded by the presence of LLJs within 2 hours, establishing nocturnal rainfall influenced by LLJs as a major component of warm-season rainfall in China. This relationship was strongly modulated by the seasonal migration of the western Pacific subtropical high (WPSH), whose northward progression and subsequent retreat governed the latitudinal displacement of HR belts and closely synchronized with the spatiotemporal evolution of LLJ activity. The proportion of nocturnal rainfall events associated with LLJs during the four rainy season phases reached 60.4%, 56.3%, 49.4%, and 54.9%, respectively (solid-filled bars in Fig. 4a). Among 841 identified nocturnal HR events nationwide, 33.9%–47.2% were classified as LLJ_HR events across the four phases (diagonally striped bars in Fig. 4a). This contrast between the high LLJ association for general nocturnal rainfall and the more moderate fraction for HR indicates that, although LLJs are a frequent precursor to rainfall, their presence alone does not guarantee the occurrence of heavy rainfall.

A more detailed statistical analysis of ROIs revealed the key role of LLJ coupling in primary rain belt regions of each phase. A total of 71, 49, 33, and 34 nocturnal HR events were identified in these ROIs during the period from Phase 1 to Phase 4 (Fig. 4b). On average, nearly 45.0% of HR events in these regions were associated with LLJs within 2 hours before onset. Spatial analysis further confirmed that these LLJ_HR events consistently produced heavier rainfall intensities than non-LLJ_HR events (red boxes in Fig. 5), particularly within the four ROIs (red boxes in Fig. 5). Nevertheless, the non-LLJ_HR events exhibited spatially heterogeneous intensity distributions, where localized maxima may occur in areas outside the primary rain belts. For instance, during Phase 2 in ROI-3 (Fig. 5f), sporadic high-intensity events driven by deep cold

trough system resulted in high site-averaged intensities even without LLJs, whereas in ROI-2, the absence of LLJs typically corresponded to weaker frontal precipitation (Fig. S6).

Furthermore, at the national scale, probability distributions of rainfall intensity (Fig. 6) indicated that LLJ_HR events exhibited a significantly higher tail (≥ 2.0 mm/6 min) compared to non-LLJ_HR events during Phases 1 and 3. During Phases 2 and 4, however, the distributions of the two event types were comparable, with LLJ_HR events showing slightly weaker intensities. Regionally, rainfall intensities within the key ROIs generally exceeded the national average, particularly for LLJ_HR events. Specifically, ROI-1 and ROI-2 demonstrated significantly higher probabilities of heavier rainfall (≥ 2.0 mm/6 min) in LLJ_HR events. Notably, LLJ_HR events in ROI-4 favored intensities near 0.5 and 2.8 mm/6 min, yet the overall probabilities of heavier rainfall remained slightly lower than non-LLJ_HR events. Despite the relatively high frequency of LLJ_HR events in ROI-3 during Phase 3 (see the pie charts in Fig. 6), their probability of producing heavier rainfall was comparable to—rather than substantially greater than—that of non-LLJ_HR events. Moreover, this region exhibited the sharpest decay in probability density for heavier rainfall among all regions. This behavior suggests that, although LLJs occur frequently in this region and season, their contribution to extreme rainfall intensity is not dominant. Instead, other non-LLJ forcing mechanisms, such as topographic lifting and mesoscale convective systems, may play an equally or more significant role in generating HR in ROI-3 during Phase 3.

In summary, although LLJ_HR events were generally associated with enhanced rainfall intensities across most ROIs and most phases, only ~31.1% of all identified LLJ events were ultimately classified as HR events (Fig. 4b). This relatively low conversion rate indicates that the mere presence of LLJs is not sufficient to produce HR. The substantial number of LLJ_non-HR events implies that additional dynamic and thermodynamic conditions must coexist with LLJs to trigger HR. In particular, factors such as moisture transport efficiency, vertical wind shear configuration, atmospheric stability, and mesoscale lifting mechanisms may modulate whether an LLJ evolves into

a heavy-rain-producing system. Therefore, a detailed further examination of the fine-scale vertical structures of LLJs prior to rainfall onset is crucial to disentangle the dynamical characteristics that distinguish HR-producing LLJs from non-HR cases, as explored in the following sections.

3.2 Minute-scale evolution of LLJs preceding nocturnal heavy and non-heavy rainfall

To elucidate the contrasting precursor characteristics of LLJs that lead to nocturnal rainfall of differing intensities, this section examines fine-scale vertical structure and continuous evolution of LLJs within 2 hours preceding both LLJ_HR and LLJ_non-HR events during four phases in their respective ROIs. The results revealed the distinct spatiotemporal variations in vertical structure and evolutionary patterns of LLJs occurred across seasonal phases.

During Phase1 in ROI-1, LLJ_HR events exhibited a significant increase in frequency starting 108 min before rainfall onset, reaching secondary peaks at –84 min and –60 min, culminating in maximum frequency immediately preceding HR (Fig. 7a). Meanwhile, the average wind profiles showed a rapid intensify trend from 48 min before HR onset, with the jet core reaching its peak wind speed (about 12.2 m s^{-1}) and its height distinctly decreased (Fig. 8a), although there is the transient weakening of jet strength within 60–48 min preceding HR. These LLJs featured a bimodal vertical distribution with frequent occurrence layers at 0.5–1 km and 1.5–2 km AGL. This structure was characteristic of double low-level jets (DLLJs), where the coexistence of the boundary layer jets (BLJs) and synoptic-system-related jets (SLLJs) generated a deep layer of forced ascent via BLJ-exit convergence and SLLJ-entrance divergence. This dynamical coupling significantly favors organized deep convection in ROI-1 (Uccellini and Johnson, 1979; Du and Chen, 2018; Du and Chen, 2019; Liu et al., 2020). Note that the composite wind profile (Fig. 8a) does not show a distinct bimodal vertical distribution due to smoothing from averaging. Detailed examination of wind profiles revealed that approximately 40% of LLJ_HR events exhibited DLLJs, while only 20% of LLJ_non-HR events showed such a structure. Therefore, LLJ_non-HR events lacked

this dynamic coupling, with jets predominantly confined to the single 0.5–1 km layer. Although LLJ_non-HR events showed a gradual increase in frequency from –48 min, along with strengthening winds prior to rainfall (Figs. 7e and 8e), these changes were rather limited compared to the pronounced evolution seen in LLJ_HR events under a background of overall lower frequency and weaker intensity. This steady and weak dynamical structure failed to provide sufficient dynamic lifting to efficiently initiate strong convection.

Both event types exhibited notably high frequencies and intensities of LLJs over ROI-2 during Phase 2, yet their evolutionary dynamics diverged sharply. For LLJ_HR events, a coherent oscillatory vertical reorganization of LLJs is evident (Figs. 7b and 8b). At the first stage, both LLJ frequency and wind speed maximum peaked (exceeding 12 m s^{-1}) at –120 min, with the core situated 1.5–2 km AGL. Subsequently, a rapid descent of frequently occurring height of LLJs to below 1 km AGL occurred, accompanied by a concurrent decline in frequency and profile intensity to a minimum around 84–72 min preceding HR. Analysis of wind kinetic energy and its vertical transport (see Eqs. 1 and 2 in supporting material) confirmed that the 'sudden drop' likely results from the downward momentum transfer (Fig. S7a and c), which can efficiently enhance low-level disturbances and dynamic forcing and serve as an effective indicator of HR 1–2 hours later (Liu et al. 2003; Fu et al., 2020). Following this descent, a distinct recovery phase ensued from –60 min, where the frequency increased reaching a secondary peak at –48 min and jet core re-ascended to 1–2 km AGL. The LLJ profile strength re-intensified to about 11.4 m s^{-1}. This rise of the jet core and secondary enhancement are likely tied to cold pool-LLJ interactions and intensified upward motion or latent heat release in convective clouds (further discussed in Section 3.3). In conclusion, this pattern suggests an intense internal dynamical adjustment process. In comparison, LLJ_non-HR events lacked such low-level momentum transfer signals (Fig. S7b and d) and maintained a quasi-steady state, with consistent LLJs strength (near 11.8 m s^{-1}) and a preferred height range of 1–2 km AGL (Fig. 8f). The LLJs frequency exhibited gradual changes, peaking weakly at 36 min preceding rainfall before a subsequent rapid decrease (Fig. 7f). This pattern indicates

an absence of the rapid dynamical redistribution observed in LLJ_non-HR events.

During Phase 3 in ROI-3, LLJ_HR events exhibited a bimodal temporal distribution in LLJ frequency, with prominent peaks at –96 min and –48 min (Fig. 7c). The dominant LLJ height was centered between 1–1.5 km AGL. The wind profiles showed a corresponding evolution where the maximum wind speed increased from approximately 8.0 m s^{-1} at –120 min to a first peak about 9.5 m s^{-1} by –84 min. Following a transient weakening (–48 to –24 min), a secondary intensification occurred immediately preceding HR onset (Fig. 8c). Conversely, LLJ_non-HR events were characterized by substantially lower LLJs frequency (around 20%) and a more diffuse structure (Fig. 7g), with wind profiles exhibiting weaker intensification preceding rainfall (Fig. 8g). Consequently, the rapid reorganization and final intensification of LLJs appeared to be critical dynamical drivers for HR. However, despite the potential influences of regional thermodynamics and topography, the insufficient dynamical forcing from overall weaker wind profiles in ROI-3 remained the primary reason for its comparatively lower probability of heavier rainfall ($\geqslant$2.0 mm/6 min).

During Phase 4 in ROI-4, LLJ_HR events exhibited a distinctive two-stage intensification process. The wind profiles initially strengthened rapidly starting from -120 min, reaching a primary peak of approximately 12.8 m s^{-1} at –72 min (Fig. 8d), coinciding with a secondary peak in LLJ frequency. Following a brief weakening (–60 to –48 min), a renewed and explosive intensification occurred from –48 min onwards, continuing until rainfall onset. Throughout this period, the LLJ cores remained concentrated between 0.5–1.5 km AGL (Fig. 7d). In sharp contrast, LLJ_non-HR events displayed a pattern of premature peaking followed by decay. Both frequency and intensity peaked earlier at –84 min, followed by general attenuation (Fig. 7h). By –48 min, weakened wind profiles stabilized into a double-core structure maintaining around 10 m s^{-1}, with distinct jet cores near 0.8 km and 1.7 km AGL (Fig. 8h). Crucially, in the LLJ_non-HR event, this premature peak and the subsequent continuous attenuation of the low-level wind field resulted in a lack of sustained dynamic forcing during the critical pre-rainstorm stage, failing to trigger HR.

Synthesizing the evolution across all phases, although a distinct transient weakening of the jet profile was consistently observed, LLJs exhibited a rapid re-intensification of wind speed accompanied by a lowering of the jet core height during approximately the final 30 min preceding HR. This recurring pre-rainfall adjustment suggests that LLJs underwent a short-term dynamical reorganization prior to HR onset. We propose that this minute-scale oscillatory behavior—characterized by a 'weakening-then-strengthening' or 'descent-then-ascent' pattern—constitutes a robust dynamic precursor of HR. Physically, the temporary weakening may reflect momentum redistribution or enhanced turbulent mixing, whereas the subsequent intensification and descent of the jet core likely enhance low-level moisture convergence and vertical wind shear, thereby strengthening upward motion and promoting convective development (Markowski & Richardson, 2010). Such rapid structural adjustment indicates that the timing and vertical evolution of LLJs, rather than their mere presence, play a critical role in modulating heavy rainfall production.

Furthermore, probability distributions of LLJ strength and height within 2 hours preceding rainfall were compared across key regions (Fig. 9). During Phase 1 in ROI-1, the strength of LLJs in LLJ_HR events was notably stronger by 2–3 m s^{-1} than that in LLJ_non-HR events (Fig. 9a). Height distributions showed distinct bimodal peaks near 0.9 km and 1.75 km AGL (Fig. 9e). The average LLJs height was generally higher in LLJ_HR events, which is usually affected by the coupling of the upper-level jet stream or the land-sea breeze. During Phase 2 in ROI-2, LLJ_HR events showed higher probabilities of strong LLJs (17–28 m s^{-1}) compared to the dominant 13 m s^{-1} intensity in LLJ_non-HR events (Fig. 9b). Influenced by large-scale circulation patterns, both event types featured LLJs centered near 1.5 km AGL (Fig. 9f), though LLJ_HR events developed a secondary maximum near 0.8 km AGL due to pre-rainfall descent of the jet core (Fig. 7b). Contrastingly, Figure 9c shows that LLJ_HR events were associated with weaker jet strengths (around 11 m s^{-1}) compared to LLJ_non-HR events (14–23 m s^{-1}) in ROI-3 during Phase 3, suggesting that strong LLJs don't necessarily induce HR here. The height of LLJ in LLJ_HR events mainly concentrated near 1.2 km AGL, whereas in LLJ_non-HR events, it was more uniformly distributed between 0–3 km

AGL with a higher probability nearly 1.5 km (Fig. 9g). For Phase 4 in ROI-4, LLJs strength peaked near 15 m s^{-1} in both event types, but LLJ_HR events featured stronger jets reaching 25–30 m s^{-1} (Fig. 9d). The LLJs height in both events peaked predominantly at 0.8 km AGL, with secondary peaks at 1.5 km for LLJ_HR and 2.0 km AGL for LLJ_non-HR events (Fig. 9h).

In summary, although different internal dynamic adjustments, including frequency, occurrence height, and wind profile intensity of LLJs, preceding LLJ_HR events were observed due to the different dominant mechanisms influencing rainfall in each phase, our findings highlight the role of fine-scale LLJ structures and their rapid vertical reorganization in modulating nocturnal rainfall intensity, offering valuable insights for improving regional nocturnal HR forecasting.

3.3 Thermodynamic evolution associated with LLJs preceding nocturnal heavy and non-heavy Rainfall

The section 3.2 has clarified that the fine-scale dynamic characteristics of LLJs—including their temporal evolution, vertical structure and intensity variations—play a pivotal role in modulating nocturnal rainfall intensity during rainy season phases. However, the influence of LLJs on rainfall generation and intensification rarely operates in isolation; instead, it depends strongly on the accompanying large-scale thermodynamic environment, which provides the necessary moisture supply and convective instability to sustain or amplify heavy rainfall. Thus, to fully unravel the mechanisms underlying the distinction between LLJ_HR and LLJ_non-HR events, it is essential to complement the dynamic analysis with an in-depth examination of the thermodynamic conditions associated with LLJs within the immediate pre-convective environment (within 1-hour preceding rainfall).

Further analysis of the large-scale thermodynamic conditions at 1 hour prior to rainfall onset (Figs. 10 and 11) reveals consistently stronger thermal instability for LLJ_HR versus LLJ_non-HR events, accompanied by stronger MFC within key regions during each rainy season.

During Phase 1 in ROI-1, thermodynamic conditions were comparable between event types. Southwesterly LLJs transported warm-moist air masses from the South China Sea and Bay of Bengal, forming a pronounced warm-humid tongue (Fig. 10a and 10e). Coupled with MFC centers developing north of the jet axis (Fig. 11a and 11e), this configuration facilitated nocturnal rainfall development. During Phase 2 in ROI-2, LLJ_HR events exhibited a significantly stronger warm-moisture tongue with core θ_e reaching 358 K—approximately 2 K higher than in non-HR events (Figs. 10b and 10f). Dynamically, the stronger LLJ core (difference >1.2 m s^{-1}) drove a sharper, continuous band of MFC along the left flank of the jet axis (Fig. 11b), creating a robust triggering mechanism for HR (Fig. 11b). During Phase 3 in ROI-3, intensified southwesterly LLJs in HR events drove substantial northward transport of abundant moisture and higher θ_e air (difference >2 K) northward into a low θ_e environment (Fig. 10c), enhancing convective instability. The synergistic interaction of this moist, high-energy advection with orographic forcing from the Taihang Mountains generated intense MFC, with peak values south of Beijing approximately 30×10^{-5} km m^{-2} s^{-1} (Fig. 11c) larger than those in LLJ_non-HR events, thereby driving nocturnal HR. Thermodynamic contrasts were most pronounced during Phase 4 in ROI-4. Thermodynamic contrasts were most pronounced during Phase 4 in ROI-4. LLJ_HR events featured a deep high-θ_e region (>356 K) over the southeastern Tibetan Plateau (Fig. 10d), contrasting with the cold highs located to the northeast of ROI-4 and lower θ_e prevalent in LLJ_non-HR events (Fig. 10h). Concurrently, accelerated easterly-southeasterly LLJs drove warm, moist air towards the steep eastern Plateau margin. The impingement of this flow against the sharp topographic gradient generated intense dynamic lifting and low-level convergence. This mechanically forced ascent, synergizing with the abundant moisture transport and strong MFC (Fig. 11h), played an essential role in triggering the observed nocturnal HR in this region.

To elucidate the rapid processes leading to occurrence of rainfall, the minute-scale evolution of key thermodynamic and dynamic parameters was further analyzed (Fig. 12), including surface θ_e, LLJ index and VWS. Specifically, LLJ index is defined as the ratio of maximum wind speed below 3 km to the height where wind first exceeds 10 m

s^{-1}. A rapid rise in LLJ index will reflect the extension and pulsing intensity of the LLJ, and its magnitude has been shown to be positively correlated with subsequent rainfall intensity 1–2 hour later (Liu et al., 2003). VWS is calculated as the wind speed difference between the surface and jet height divided by the jet height and is used to characterize the bulk shear from the surface to the jet layer associated with the dynamical forcing and organization of convection (Wei et al., 2014).

Figure 12a illustrated that during Phase 1 in ROI-1, despite the similarity in large-scale environments between LLJ_HR and LLJ_non-HR events, they exhibited distinct differences in the continuous evolution of LLJ-associated thermodynamic conditions preceding rainfall onset. LLJ_HR events exhibited abrupt thermodynamic enhancement from 90 min preceding the onset of rainfall driven by rapid intensification of LLJs, with surface θ_e and VWS surging approximately 1.5 K and 0.005 s^{-1} respectively. Concurrently, the LLJ index surged from approximately 0.05 to 0.08 and VWS peaked sharply at –60 min, signaling LLJs intensification and core descent (Figs. 7a, 8a). This rapid, minute-scale co-intensification of thermodynamic and dynamic processes serves as a critical precursor triggering HR. In contrast, LLJ_non-HR events showed weaker increases of θ_e and VWS and a declining LLJ index (by about 0.02) alongside rising jet cores, reducing low-level shear and convergence efficiency, thereby diminishing overall rainfall intensity.

During Phase 2 in ROI-2, the thermodynamic environment displayed a distinct 'weakening-reintensification' pattern (Fig. 12b), which aligns precisely with the intrinsic dynamical adjustments of the wind field presented in Fig. 8b. Initially, at -120 min, concurrent peaks in the LLJ index and VWS were observed, coupled with a high surface θ_e of 348.3 K. During the subsequent transition period, a drastic elevation in the jet core height starting from -84 min caused a precipitous drop in the LLJ index. The timing of this rapid evolution suggests a transient optimal window for nocturnal rainfall triggering that is characteristic of LLJ_HR events in ROI-2. Following this, rapid surface cooling began 60 min prior to HR. This cooling was likely induced by the cold pool outflows associated with alternation or propagation of convective systems embedded within the Mei-Yu front cloud system (Zhang et al., 2023). The resulting

dense cold air wedging beneath the strong southwesterly LLJs can lift the jet axis above the cold-pool interface, further enhancing uplift and promoting rainfall (Luo et al., 2014). This in turn facilitated the final re-intensification of the jet structure (Fig. 7b and 8b). Crucially, this reorganized configuration sharply enhances low-level vertical wind shear and horizontal convergence (Fig. 12b), further promoting HR development. In contrast, LLJ_non-HR events exhibited weaker thermodynamic support and diminished dynamic forcing with consistently lower LLJ indices within 60 min preceding rainfall, resulting in insufficient lift to sustain HR. Compared with the disordered fluctuations of the LLJ_non-HR events, LLJ_HR events highlight the importance of thermal-dynamic synergy influenced by LLJs evolution. Even though the LLJ evolution may be modulated by convective feedback, the resulting reorganized jet profile still can serve as a robust dynamical precursor essential for triggering local HR.

During Phase 3 in ROI-3, LLJ_HR events featured prominent thermal compensation (surface $\Delta\theta_e$ > 1K, 850hPa $\Delta\theta_e$> 2K versus non-HR events)—despite possessing generally weaker dynamical forcing compared to other phases (Fig. 12c). Temporally, the evolution was marked by distinct pulsations: The LLJ index exhibited a rapid rise (from ~0.03 to ~0.06) starting 84 min prior to HR onset (Fig. 12c) driven by a surge of LLJs profiles, while VWS peaked synchronously with the maximum LLJ frequency. Subsequently, a secondary peak in both the LLJ index and VWS was observed between –60 and –48 min. Although the subsequent declines in wind speed and frequency led to notable fluctuations in these parameters, the VWS and LLJ index underwent substantial intensification (with VWS increasing by ~1.5 s^{-1}) in the final 24 min, driven by the rapid acceleration of the LLJ wind field. This co-evolution with rapid surface warming (increase of 0.25 K) released convective instability and enhanced convergence (Fig. 10). Nevertheless, the overall weaker dynamical conditions likely limited the depth and organization of convection, potentially accounting for the reduced probability of heavier rainfall compared to other phases. In contrast, during LLJ non-HR events, the LLJ index (~0.03) and θ_e vary rather gradually.

During Phase 4 in ROI-4, under the favorably thermal environments (θ_e > 346 K), LLJ_HR events showed a two-stage dynamic intensification. Initially, the LLJ index

surged, while the VWS and jet intensity reached synchronous secondary peaks at –72 min. In the second stage, VWS increased rapidly by ~0.9 (Fig. 12d), and the LLJ index maintained an overall upward trend, peaking immediately prior to onset due to the surging jet. But LLJ_non-HR events showed weakening trends in both dynamic and thermodynamic conditions during the final 30 min and exhibited weaker changes (ΔVWS < 0.45 s^{-1}, ΔLLJ index < 0.02), reflecting an absence of the coordinated intensification necessary to initiate and sustain HR.

Although the evolution paths of the thermodynamic environment vary across different phases, a universal cross-region precursor emerges: the LLJ index and VWS consistently exhibits a strengthening or stabilizing trend in the final approximately 30 min preceding HR onset, operating in concert with significant low-level warming (rising θ_e). In contrast, non-HR events generally lack this culminating dynamical intensification. Overall, these results adequately showcase the sensitivity of regional HR to the fine-scale structural evolution of LLJs and their coupling with thermodynamic environments.

4. Summary and concluding remarks

Using wind profile measurements from a nationwide network of 31 RWPs during the warm seasons (April–October) of 2023–2024, this study characterized the minute-scale evolution of LLJs as dynamic precursors to nocturnal rainfall across China. By systematically comparing the vertically resolved structure and temporal evolution of LLJs within the 2-hour window preceding nocturnal HR and non-HR events across four distinct rainy-season phases, we identified the key dynamic-thermodynamic distinctions governing rainfall intensity.

At the national scale, nocturnal rainfall accounted for nearly half of the total warm-season precipitation, and 56% of nocturnal rainfall events were preceded by LLJs within 2 hours. In the key regions of interest (ROIs), approximately 45.0% of identified HR events were associated with LLJs. Overall, LLJ-related events were significantly more prone to producing heavier rainfall than non-LLJ events across most regions, underscoring the strong coupling between LLJs and nocturnal HR.

Despite regional differences in synoptic forcing, consistent contrast in LLJ evolution were observed between HR and non-HR events across all phases. During Phase 1 in ROI-1, a bimodal vertical distribution of LLJs and their rapid thermodynamic-dynamic co-intensification starting 84 min prior to rainfall were identified as key precursors of LLJ_HR events, in sharp contrast to the decoupled dynamics of LLJ_non-HR events. Phase 2 (ROI-2) was characterized by a distinct oscillatory process, where HR events featured a rapid descent of the LLJ core below 1 km followed by a robust rebound, distinguishing them from the quasi-steady state of LLJ_non-HR cases. In Phase 3 (ROI-3), LLJ_HR events exhibited significant thermal compensation and bimodal pulsations (peaks at –96 and –48 min), with a critical final-stage intensification serving as the decisive trigger. Similarly, Phase 4 (ROI-4) featured a distinctive two-stage intensification, where a rapid LLJ surge within 48 min of onset distinguished LLJ_HR events from the significantly attenuated dynamical structures of LLJ_non-HR events.

Although the detailed dynamical pathways vary among phases, a unifying feature emerges: all LLJ_HR events exhibit a 'final-stage intensification' of low-level dynamics —manifested as enhanced LLJ strength, vertical wind shear, and LLJ index— within approximately 30 min preceding rainfall, occurring in synergy with increasing thermodynamic instability (e.g., rising equivalent potential temperature, θ_e). This result confirms the universality of the final-stage low-level dynamic amplification identified in our previous study (Li et al., 2024) and demonstrates its national-scale applicability across diverse monsoon regimes.

Crucially, this study further identifies a previously under-resolved "preparatory adjustment" phase occurring 30–120 minutes prior to rainfall onset, during which LLJ frequency, strength and core height undergo systematic minute-scale reorganization. This national-scale evidence indicates that the final dynamic trigger is contingent upon this earlier synergistic coupling of minute-scale jet structural evolution and thermodynamic destabilization. This rapid, synergistic reorganization represents a necessary precondition for HR generation and contrasts sharply with the comparatively steady evolution observed in LLJ_non-HR events. These results highlight that the

occurrence and intensity of nocturnal rainfall are governed not simply by LLJ presence, but by the fine-scale vertical evolution of LLJs and their interaction with regional thermodynamic conditions.

Overall, this study establishes robust dynamic-rainfall linkages associated with LLJs across different warm-season rainy periods in China. Future research should: (1) expand multi-source observations to establish dynamic thresholds for early forecasting systems of nocturnal rainfall, and (2) develop quantitative frameworks relating LLJ structural evolution to rainfall intensity, offering theoretical support for optimizing physical processes in LLJ parameterization schemes within high-resolution numerical models. Further investigation is also needed to clarify the physical mechanisms controlling rapid adjustments in LLJ core height and strength immediately prior to rainfall onset.

Data Availability

The LLJs retrieved from the RWP network can be acquired from https://doi.org/10.5281/zenodo.17176759 (Li and Guo, 2025). The data from the weather station are obtained from the China Meteorological Data Service Centre at https://data.cma.cn/en, and the original ERA5 reanalysis data used here are available from the ECMWF in Hersbach et al. (2020).

Acknowledgments

This work was supported by the National Natural Science Foundation of China under grant 42325501, the Science and Technology Supporting Project of Guizhou Province ([2023]236) and the National Key Research and Development Program of China under grant 2024YFC3013001. Last but not least, we appreciated tremendously the constructive comments and suggestions made by the anonymous reviewers that significantly improved the quality of our manuscript.

Author Contributions

The study was completed with close cooperation between all authors. JG designed the research framework; NL performed the analysis and drafted the original manuscript

with contribution from JG; JG, XG, ZZ, YZ. JG, NT, YW, and YZ helped revise the manuscript.

Completing interests

The authors declare that they have no conflict of interest.

References

Anthes, R. A., Kuo, Y. H., Benjamin, S. G., and Li, Y. F: The evolution of the mesoscale environment of severe local storms: Preliminary modeling results, Mon. Weather Rev., 110(9), 1187-1213, doi:10.1175/1520-0493(1982)110,1187: TEOTME.2.0.CO;2, 1982.

Bai, L., Chen, G., Huang, Y., and Meng, Z.: Convection initiation at a coastal rainfall hotspot in South China: Synoptic patterns and orographic effects, J. Geophys. Res. Atmos., 126(24), e2021JD034642, doi: 10.1029/2021JD034642, 2021.

Blackadar, A. K.: Boundary layer wind maxima and their significance for the growth of nocturnal inversions, Bull. Am. Meteorol. Soc., 38(5), 283-290, doi:10.1175/1520-0477-38.5.283, 1957.

Bonner, W. D.: Climatology of the low-level jet, Mon. Weather Rev., 96(12), 833-850. doi:10.1175/1520-0493(1968) 096<0833:COTLLJ>2.0.CO;2, 1968.

Cao, Q., J. Guo, C. Xue, Z. Li, H. Xu, N. Li, Y. Sun, Z. Zhang, Y. Wang, J. Chen, Y. Zhou, and T. Chen: Divergent Sounding-derived Precursor Pathways Enable Discrimination of Dry versus Wet Severe Convective Winds. Geophysical Research Letters, 52, e2025GL117491. https://doi.org/10.1029/2025GL117491, 2025.

Carbone, R. E., and Tuttle, J. D.: Rainfall occurrence in the US warm season: The diurnal cycle, J. Clim., 21(16), 4132-4146, doi:10.1175/2008JCLI2275.1, 2008.

Chen, G., Sha, W., Iwasaki, T., and Wen, Z.: Diurnal Cycle of a Heavy Rainfall Corridor over East Asia, Mon. Weather Rev., 145(8), 3365-3389, doi:10.1175/mwr-d-16-0423.1, 2017.

Chen, H., Zhou, T., Neale, R. B., Wu, X., and Zhang, G. J.: Performance of the new NCAR CAM3. 5 in East Asian summer monsoon simulations: Sensitivity to modifications of the convection scheme, J. Clim., 23(13), 3657-3675, doi:10.1175/2010JCLI3022.1, 2010.

Chen, T., Guo, J., Guo, X., Zhang, Y., Xu, H., and Zhang, D.-L.: On the multiscale processes leading to an extreme gust wind event in East China: Insights from radar

682 wind profiler mesonet observations. Journal of Geophysical Research:
683 Atmosphere, 129, e2024JD041484, doi: 10.1029/2024JD041484, 2024.
684 Chen, X., F. Zhang, and K. Zhao: Diurnal Variations of the Land-Sea Breeze and Its
685 Related Precipitation over South China. J. Atmos. Sci., 73, 4793–4815,
686 doi:10.1175/JAS-D-16-0106.1, 2016.
687 Chen, Y. L., and Li, J.: Large-scale conditions favorable for the development of heavy
688 rainfall during TAMEX IOP 3, Mon. Weather Rev., 123(10), 2978-3002, 1995.
689 China Meteorological Administration: Specification for Automatic Observation of
690 Ground Meteorology. China Meteorological Press, 2020.
691 Davis, C. A., Maning, W. K., Carbone, R., Trier, S., and Tuttle, J.: Coherence of warm-
692 season continental rainfall in numerical weather prediction models, Mon. Weather
693 Rev., 131, 2667-2679, doi:10.1175/1520-
694 0493(2003)131<2667:COWCRI>2.0.CO;2, 2003.
695 Dong, F., Zhi, X., Zhang, L., and Ye, C.: Diurnal variations of coastal boundary layer
696 jets over the northern South China Sea and their impacts on diurnal cycle of
697 rainfall over southern China during the early-summer rainy season, Mon. Weather
698 Rev., 149(10), 3341-3363, doi:10.1175/MWR-D-20-0292.1, 2021.
699 Doubler, D. L., Winkler, J. A., Bian, X., Walters, C. K., and Zhong, S.: An NARR-
700 derived climatology of southerly and northerly low-level jets over North America
701 and coastal environs, J. Appl. Meteorol. Climatol., 54(7), 1596-1619,
702 doi:10.1175/JAMC-D-14-0311.1, 2015.
703 Du, Y., and Chen, G.: Heavy Rainfall Associated with Double Low-Level Jets over
704 Southern China. Part II: Convection Initiation, Mon. Weather Rev., 147(2), 543-
705 565, doi:10.1175/mwr-d-18-0102.1, 2019.
706 Du, Y., and G. Chen: Heavy Rainfall Associated with Double Low-Level Jets over
707 Southern China. Part I: Ensemble-Based Analysis, Monthly Weather Review, 146,
708 3827–3844, doi: 10.1175/MWR-D-18-0101.1, 2018.
709 Du, Y., Chen, G., Han, B., Bai, L., and Li, M.: Convection initiation and growth at the
710 coast of South China. Part II: Effects of the terrain, coastline, and cold pools, Mon.
711 Weather Rev., 148(9), 3871-3892, doi:10.1175/MWR-D-20-0090.1, 2020.

712 Du, Y., Zhang, Q., Ying, Y., and Yang, Y.: (2012). Characteristics of low-level jets in
713 Shanghai during the 2008-2009 warm seasons as inferred from wind profiler radar
714 data, J. Meteorol. Soc. Jpn. Ser. II, 90(6), 891-903, doi:10.2151/jmsj.2012-603,
715 2012.
716 Fu, S. M., Jin, S. L., Shen, W., Li, D. Y., Liu, B., & Sun, J. H.: A kinetic energy budget
717 on the severe wind production that causes a serious state grid failure in Southern
718 Xinjiang China, Atmospheric Science Letters, 21(7), e977, 2020.
719 Gebauer, J. G., Shapiro, A., Fedorovich, E., and Klein, P.: (2018). Convection Initiation
720 Caused by Heterogeneous Low-Level Jets over the Great Plains, Mon. Weather
721 Rev., 146(8), 2615-2637, doi:10.1175/mwr-d-18-0002.1, 2018.
722 Guo, J., Liu, B., Gong, W., Shi, L., Zhang, Y., Ma, Y., Zhang, J., Chen, T., Bai, K.,
723 Stoffelen, A., de Leeuw, G., and Xu, X.: Technical note: First comparison of wind
724 observations from ESA's satellite mission Aeolus and ground-based radar wind
725 profiler network of China, Atmos. Chem. Phys., 21, 2945-2958, doi: 10.5194/acp-
726 21-2945-2021, 2021 (data available at: https://data.cma.cn, last access: 11 January
727 2024).
728 Guo, X., Guo, J., Chen, T., Li, N., Zhang, F., and Sun, Y.: Revisiting the evolution of
729 downhill thunderstorms over Beijing: a new perspective from a radar wind profiler
730 mesonet, Atmos. Chem. Phys., 24(14), 8067-8083, doi:10.5194/acp-24-8067-
731 2024, 2024.
732 Guo, X., Guo, J., Zhang, D. L., and Yun, Y.: Vertical divergence profiles as detected
733 by two wind-profiler mesonets over East China: Implications for nowcasting
734 convective storms, Q. J. R. Meteorol. Soc., 149(754), 1629-1649.
735 doi:10.1002/qj.4474, 2023.
736 Hersbach, H., Bell, B., Berrisford, P., Biavati, G., Horányi, A., Muñoz Sabater, J.,
737 Nicolas, J., Peubey, C., Radu, R., Rozum, I., Schepers, D., Simmons, A., Soci, C.,
738 Dee, D.and Thépaut, J-N.: ERA5 hourly data on pressure levels from 1940 to
739 present. Copernicus Climate Change Service (C3S) Climate Data Store (CDS),
740 doi: 10.24381/cds.bd0915c6 (Accessed on 06-05-2024), 2023.

Higgins, R. W., Yao, Y., Yarosh, E. S., Janowiak, J. E., and Mo, K. C.: Influence of the Great Plains low-level jet on summertime precipitation and moisture transport over the central United States, J. Clim., 10(3), 481-507, 1997.

Hodges, D., and Pu, Z.: Characteristics and Variations of Low-Level Jets and Environmental Factors Associated with Summer Precipitation Extremes over the Great Plains. J. Clim., 32(16), 5123-5144, doi:10.1175/JCLI-D-18-0553.1, 2019.

Holton, J. R.: The diurnal boundary layer wind oscillation above sloping terrain, Tellus, 19(2), 200-205, doi: 10.3402/tellusa.v19i2.9766, 1967.

Horinouchi, T., Matsumura, S., Ose, T., and Takayabu, Y. N.: Jet-precipitation relation and future change of the mei-yu-baiu rainband and subtropical jet in CMIP5 coupled GCM simulations, J. Clim., 32(8), 2247-2259, doi:10.1175/JCLI-D-18-0426.1, 2019.

Huang, X., Sun, J., and Liu, W.: The interaction between low-level jet evolution and severe convective rainstorms under topographic effect, Acta Meteorol. Sin., 78(4), 551-567, 2020.

Li, N., and Guo, J.: Data for wind profiles associated with LLJs obtained from RWP observations during the warm season (April-October) of 2023-2024 in China [Data set]. Zenodo. https://doi.org/10.5281/zenodo.17176759, 2025.

Li, N., Guo, J., Wu, M., Zhang, F., Guo, X., Sun, Y., Zhang Z., Liang L., Chen T.: Low-level jet and its effect on the onset of summertime nocturnal rainfall in Beijing, Geophys. Res. Lett., 51, e2024GL110840, doi:10.1029/2024GL11084, 2024.

Li, X., and Du, Y.: Statistical relationships between two types of heavy rainfall and low-level jets in South China, J. Clim., 34(21), 8549-8566, doi:10.1175/JCLI-D-21-0121.1, 2021.

Liu, B., Ma, Y., Guo, J. and Wei, G.: Boundary layer heights as derived from ground-based radar wind profiler in Beijing, IEEE Trans. Geosci. Remote Sens., 57, 8095-8104, doi:10.1109/TGRS.2019.2918301, 2019.

Liu, X., Luo, Y., Huang, L., Zhang, D. L., & Guan, Z: Roles of double low-level jets in the generation of coexisting inland and coastal heavy rainfall over south China

during the presummer rainy season, Journal of Geophysical Research: Atmospheres, 125(18), e2020JD032890, 2020.

Luo, Y., Gong, Y., and Zhang, D. L.: Initiation and organizational modes of an extreme-rain-producing mesoscale convective system along a mei-yu front in East China, Mon. Weather Rev., 142(1), 203-221, doi:10.1175/MWR-D-13-00111.1, 2014.

Maddox, R. A.: Large-scale meteorological conditions associated with midlatitude, mesoscale convective complexes, Mon. Weather Rev., 111(7), 1475-1493, 1983.

Marengo, J. A., Soares, W. R., Saulo, C., and Nicolini, M.: Climatology of the low-level jet east of the Andes as derived from the NCEP-NCAR reanalyses: Characteristics and temporal variability, J. Clim., 17(12), 2261-2280, 2004.

Markowski, P., & Richardson, Y.: Mesoscale meteorology in midlatitudes, John Wiley & Sons, 2011.

Miao, Y., Guo, J., Liu, S., Wei, W., Zhang, G., Lin, Y., and Zhai, P.: The Climatology of Low-Level Jet in Beijing and Guangzhou, China, J. Geophys. Res. Atmos., 123(5), 2816-2830. doi:10.1002/2017jd027321, 2018.

Mitchell, M. J., Arritt, R. W., and Labas, K.: A climatology of the warm season Great Plains low-level jet using wind profiler observations, Weather Forecast., 10(3), 576-591, 1995.

Molod, A., Salmun, H. and Collow, A.B.M.: Annual cycle of planetary boundary layer heights estimated from wind profiler network data, J. Geophys. Res. Atmos., 124, 6207-6221, doi:10.1029/2018JD030102, 2019.

Monaghan, A. J., Rife, D. L., Pinto, J. O., Davis, C. A., and Hannan, J. R.: Global precipitation extremes associated with diurnally varying low-level jets, J. Clim., 23(19), 5065-5084, 2010.

Pan, H., and Chen, G.: Diurnal variations of precipitation over North China regulated by the mountain-plains solenoid and boundary-layer inertial oscillation, Adv. Atmos. Sci., 36(8), 863-884, doi:10.1175/2010JCLI3515.1, 2019.

Pitchford, K. L., and London, J.: The low-level jet as related to nocturnal thunderstorms over Midwest United States, J. Appl. Meteorol., 1(1), 43-47, 1962.

799 Rasmussen, K. L., and Houze Jr, R. A.: Convective initiation near the Andes in
800 subtropical South America, Mon. Weather Rev., 144(6), 2351-2374,
801 doi:10.1175/MWR-D-15-0058.1, 2016.
802 Reif, D. Q., and Bluestein, H.: A 20-year climatology of nocturnal convection initiation
803 over the central and southern great plains during the warm season, Mon. Weather
804 Rev., 145, 1615-1639, doi:10.1175/MWR-D-16-0340.1, 2017.
805 Roots, M., Sullivan, J. T., and Demoz, B.: Mid-Atlantic nocturnal low-level jet
806 characteristics: a machine learning analysis of radar wind profiles, Atmos. Meas.
807 Tech., 18(5), 1269-1282, doi:10.5194/amt-18-1269-2025, 2025.
808 Stensrud, D. J.: Importance of low-level jets to climate: A review, J. Clim., 1698-1711,
809 1996.
810 Subrahmayam, K. V., Udupa, S. R., Kumar, K. K., Ramana, M. V., Srinivasulu, J., and
811 Bothale, R. V.: Prediction of zonal wind using machine learning algorithms:
812 Implications to future projections of Indian monsoon jets, J. Indian Soc. Remote
813 Sens., 52(2), 371-381, 2024.
814 Sun, S. Q., Zhai, G. H., and Lorenzo, D. O.: The relationship between large-scale low-
815 level jet over east asia and monsoon as well as cross-equatorial currents in
816 summer, Acta Meteorol. Sin., 1(1), 43-50, 1986.
817 Trier, J. W. Wilson, D. A. Ahijevych, and R. A. Sobash : Mesoscale vertical motions
818 near nocturnal convection initiation in PECAN, Mon. Weather Rev., 145, 2919-
819 2941, doi:10.1175/MWR-D-17-0005.1, 2017.
820 Trier, S. B., Davis, C. A., Ahijevych, D. A., Weisman, M. L., and Bryan, G. H.:
821 Mechanisms supporting long-lived episodes of propagating nocturnal convection
822 within a 7-day WRF model simulation, J. Atmos. Sci., 63(10), 2437-2461, doi:
823 10.1175/JAS3768.1, 2006.
824 Tuttle, J. D., and Davis, C. A.: Corridors of warm season precipitation in the central
825 United States. Mon. Weather Rev., 134(9), 2297-2317, doi:10.1175/MWR3188.1,
826 2006.
827 Uccellini, L. W., and D. R. Johnson: The coupling of upper and lower tropospheric jet
828 streaks and implications for the development of severe convective storms.

829 Monthly Weather Review, 107, 682-703, doi: 10.1175/1520-
830 0493(1979)107,0682:TCOUAL.2.0.CO;2, 1979.
831 Walters, C. K., Winkler, J. A., Shadbolt, R. P., van Ravensway, J., and Bierly, G. D.:
832 A long-term climatology of southerly and northerly low-level jets for the central
833 United States, Ann. Assoc. Am. Geogr., 98(3), 521-552, 2008.
834 Wang, D., Zhang, Y., and Huang, A.: Climatic features of the south-westerly low-level
835 jet over southeast China and its association with precipitation over east China,
836 Asia-Pac. J. Atmos. Sci., 49(3), 259-270, doi:10.1007/s13143-013-0025-y, 2013.
837 Wang, W. C., Gong, W., and Wei, H.: A regional model simulation of the 1991 severe
838 precipitation event over the Yangtze-Huai River valley. Part I: Precipitation and
839 circulation statistics, J. Clim., 13(1), 74-92, doi:10.1175/1520-
840 0442(2000)013<0074:ARMSOT>2.0.CO;2, 2000.
841 Weckwerth, T. M., and Wakimoto, R. M.: The initiation and organization of convective
842 cells atop a cold-air outflow boundary, Mon. Weather Rev., 120(10), 2169–2187,
843 doi:10.1175/ 1520-0493(1992)120,2169:TIAOOC.2.0.CO;2, 1992.
844 Weckwerth, T. M., Hanesiak, J., Wilson, J. W., et al.: Nocturnal convection initiation
845 during PECAN 2015, Bull. Am. Meteorol. Soc., 100(11), 2223-2239,
846 doi::10.1175/BAMS-D-18-0299.1, 2019.
847 Wei, W., Zhang, H. S., and Ye, X. X.: Comparison of low-level jets along the north
848 coast of China in summer, J. Geophys. Res. Atmos., 119(16), 9692-9706.
849 doi:10.1002/2014jd021476, 2014.
850 Weisman, M. L., Trapp, R. J., Romine, G. S., Davis, C., Torn, R., Baldwin, M., Bosart,
851 L., Brown, J., Coniglio, M., Dowell, D., Evans, A. C., Galarneau, T. J., Haggerty,
852 J., Hock, T., Manning, K., Roebber, P., Romashkin, P., Schumacher, R., Schwartz,
853 C. S., Sobash, R., Stensrud, D., and Trier, S. B.: The mesoscale predictability
854 experiment (MPEX), Bull. Am. Meteorol. Soc., 96(12), 2127-2149,
855 doi:10.1175/bams-d-13-00281.1, 2015.
856 Whiteman, C. D., Bian, X., and Zhong, S.: Low-level jet climatology from enhanced
857 Rawinsonde observations at a site in the southern Great Plains, J. Appl. Meteorol.,

858 36(10), 1363-1376, doi:10.1175/1520-
859 0450(1997)036%3C1363:LLJCFE%3E2.0. CO;2, 1997.
860 Xia, R., and Zhao, S.: Diagnosis and modeling of meso-scale systems of heavy rainfall
861 in warm sector ahead of front in South China (middle part of Guangdong province)
862 in June 2005, Chin. J. Atmos. Sci., 33(3), 2009.
863 Xue, M., Luo, X., Zhu, K., Sun, Z., and Fei, J.: The controlling role of boundary layer
864 inertial oscillations in Meiyu frontal precipitation and its diurnal cycles over
865 China, J. Geophys. Res. Atmos., 123(10), 5090-5115,
866 doi:10.1029/2018JD028368, 2018.
867 Yan, Y., Cai, X., Wang, X., Miao, Y., and Song, Y.: Low-level jet climatology of China
868 derived from long-term radiosonde observations, J. Geophys. Res. Atmos.,
869 126(20), e2021JD035323, doi:10.1029/2021JD035323, 2021.
870 Yu, R., Li, J., Chen, H., and Yuan, W.: Progress in studies of the precipitation diurnal
871 variation over contiguous China, J. Meteorol. Res., 28(5), 877-902,
872 doi:10.1007/s13351-014-3272-7, 2014.
873 Zamora, R.J., Shapiro, M.A. and Doswell, C.A., III.: The diagnosis of upper
874 tropospheric divergence and ageostrophic wind using profiler wind observations,
875 Mon. Weather Rev., 115, 871-884, doi:10.1175/1520-0493(1987)1152.0.CO;2,
876 1987.
877 Zhang, F., Zhang, Q., Sun, J., and Xu, J.: Convection initiation during the Meiyu
878 environment in the Yangtze-Huai River basin of China, J. Geophys. Res. Atmos.,
879 128(9), e2022JD038077, doi:10.1029/2022JD038077, 2023.
880 Zhang, M., and Meng, Z.: Warm-sector heavy rainfall in southern China and its WRF
881 simulation evaluation: A low-level-jet perspective, Mon. Weather Rev., 147(12),
882 4461-4480, doi:10.1175/MWR-D-19-0110.1, 2019.
883 Zhang, Y., Xue, M., Zhu, K., and Zhou, B.: What is the main cause of diurnal variation
884 and nocturnal peak of summer precipitation in Sichuan Basin, China? the key role
885 of boundary layer low-level jet inertial oscillations, J. Geophys. Res. Atmos.,
886 124(5), 2643-2664, doi:10.1029/2018jd029834, 2019.

887 Zhao, Y., Liao, J., Zhang, Q., Chen, J., Gong, X., Shi, Y., Shi, M., Yang, D., Fan, S.,
888 Zhou, X., Cao, L., and Hu, K.: Development of China Ground Climate Normal
889 Value Dataset from 1991 to 2020, Chinese Journal of Atmospheric Sciences (in
890 Chinese), 48(2), 555–571, doi:10.3878/j.issn.1006-9895.2204.22010, 2024.
891
892

893 Table 1. Table of Representative Radar Wind Profiler Stations in Mainland China

Region	Station		Longitude (°)	Latitude (°)	Altitude (m)
ROI-1	58839	MQ	118.86	26.22	160.70
	59046	LZ	109.46	24.36	314.40
	59137	JJ	118.54	24.81	124.80
	59287	GZ	113.48	23.21	65.00
	59758	HK	110.25	19.99	69.00
ROI-2	57461	YC	111.36	30.74	253.80
	57687	CS	112.79	28.11	119.00
	57793	YCN	114.36	27.79	132.00
	58238	BJ	118.90	31.93	40.60
	58321	HF	117.03	31.57	50.00
	58367	LH	121.47	31.18	5.00
	58459	XS	120.29	30.18	48.80
ROI-3	53463	HHHT	111.68	40.82	1152.10
	53772	TY	112.58	37.62	785.00
	54511	BJ	116.47	39.81	31.50
	54534	TS	118.10	39.65	23.20
	54602	BD	115.48	38.73	16.80
ROI-4	57816	GY	106.73	26.59	1197.60
	56290	XD	104.18	30.77	514.00
	56651	LJ	100.22	26.85	2382.40
Other stations	50936	BC	122.47	45.36	156.00
	51463	WLMQ	87.65	43.79	935.00
	51628	AKS	80.38	41.12	1107.10
	52754	GC	100.08	37.2	3301.50
	52889	LZ	103.89	36.06	1519.20
	57516	CQ	106.46	29.57	260.00
	53845	YA	109.45	36.58	1180.40
	54342	SY	123.51	41.73	50.00
	54857	QD	120.13	36.23	12.00
	55664	DR	87.07	28.63	4302.00
	57171	PDS	113.12	33.77	142.00

Figures

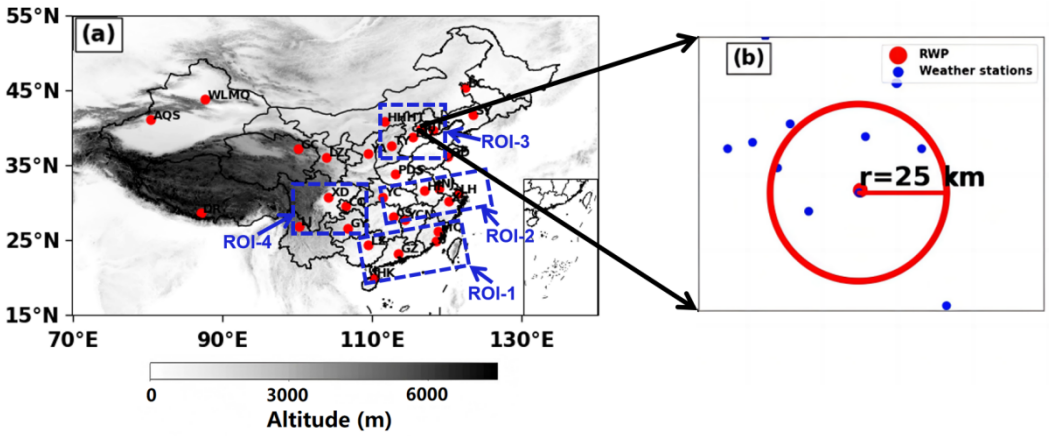

Figure.1 (a) Spatial distribution of 31 Radar Wind Profiler (RWP) stations (red dots) across China, with four regions of interest (ROIs) demarcated by blue dashed boxes: ROI-1, ROI-2, ROI-3, and ROI-4. (b) Schematic of spatial co-location: Beijing Observatory's RWP (red circle) and rain gauges (blue dots) within a 25-km radius

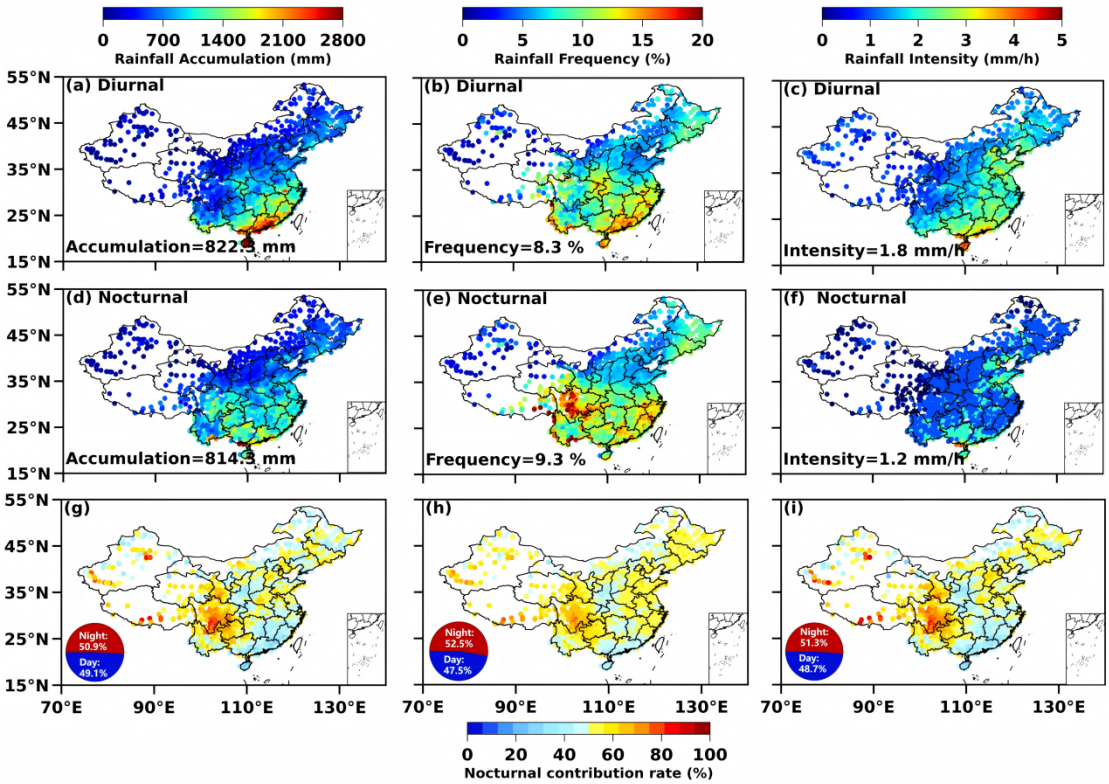

Figure 2. (a–c) Spatial distributions of accumulated rainfall (mm), rainfall frequency (%) and rainfall intensity (mm/h) in the daytime from April to October in 2023–2024. The numbers in the upper left corner represent the national average; (d–f) the same as (a–c), but in the nighttime; (g–i) Nocturnal contribution ratios of accumulated rainfall, frequency, and occurrence frequency of heavy rainfall (>75th percentile intensity). The pie charts illustrate the relative contribution rates of daytime (blue) and nighttime (red) at the national scale

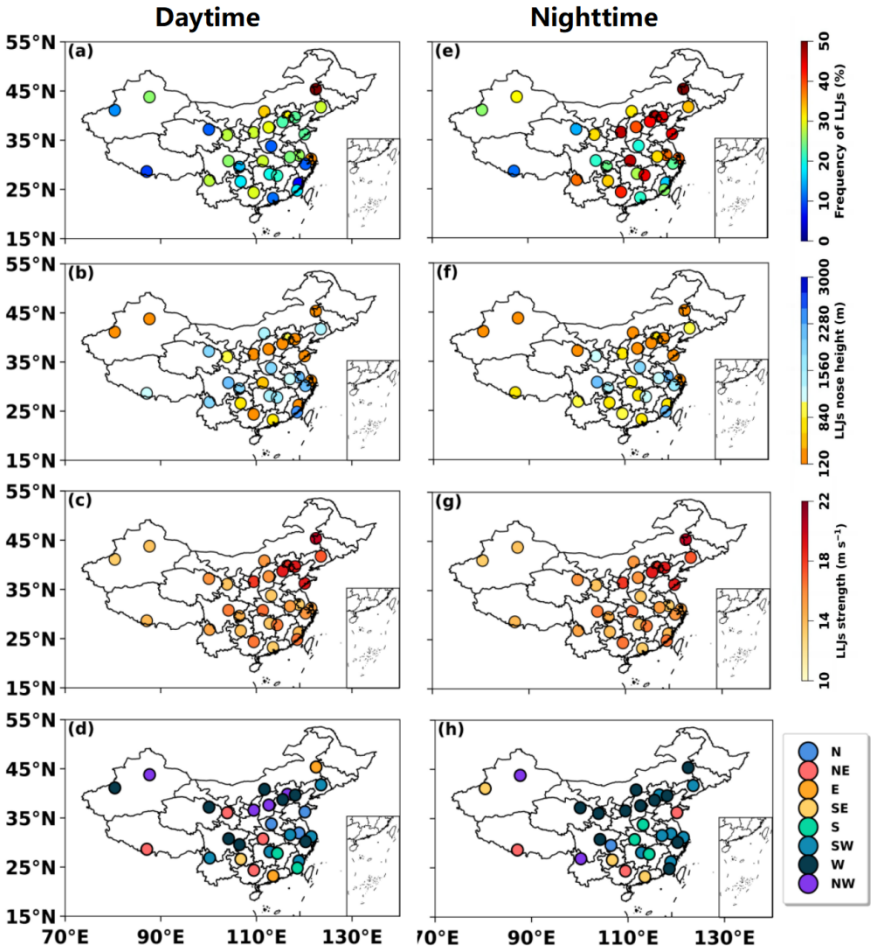

925

926 Figure 3. (a–d) Spatial distribution of occurrence frequency, height, strength, and the
927 dominant wind direction of LLJs observed by 31 RWP stations during April–October
928 from 2023 to 2024 in the daytime. (e–h) Same as (a–d), but in the nighttime.

929

930

931

932

933

934

935

936

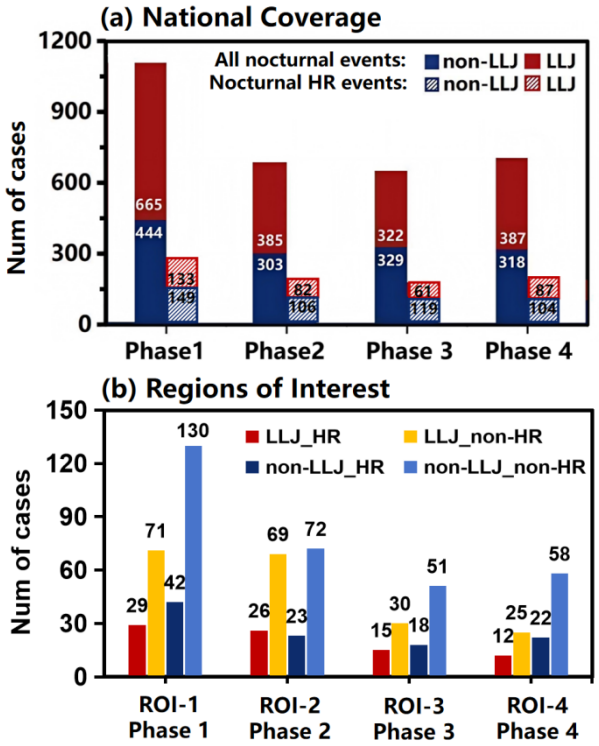

937

938 Figure 4. Statistics of all nocturnal rainfall events (solid-filled bars) and nocturnal heavy
939 rainfall (HR; diagonally striped bars) events across China during four phases,
940 categorized into LLJ events (red) and non-LLJ events (blue). (b) Statistics of nocturnal
941 rainfall events within the four ROIs (ROI-1 to ROI-4) during their corresponding
942 phases, categorized into four types: LLJ_HR (red), LLJ_non-HR (yellow), non-
943 LLJ_HR (dark blue), and non-LLJ_non-HR (light blue) events.

944

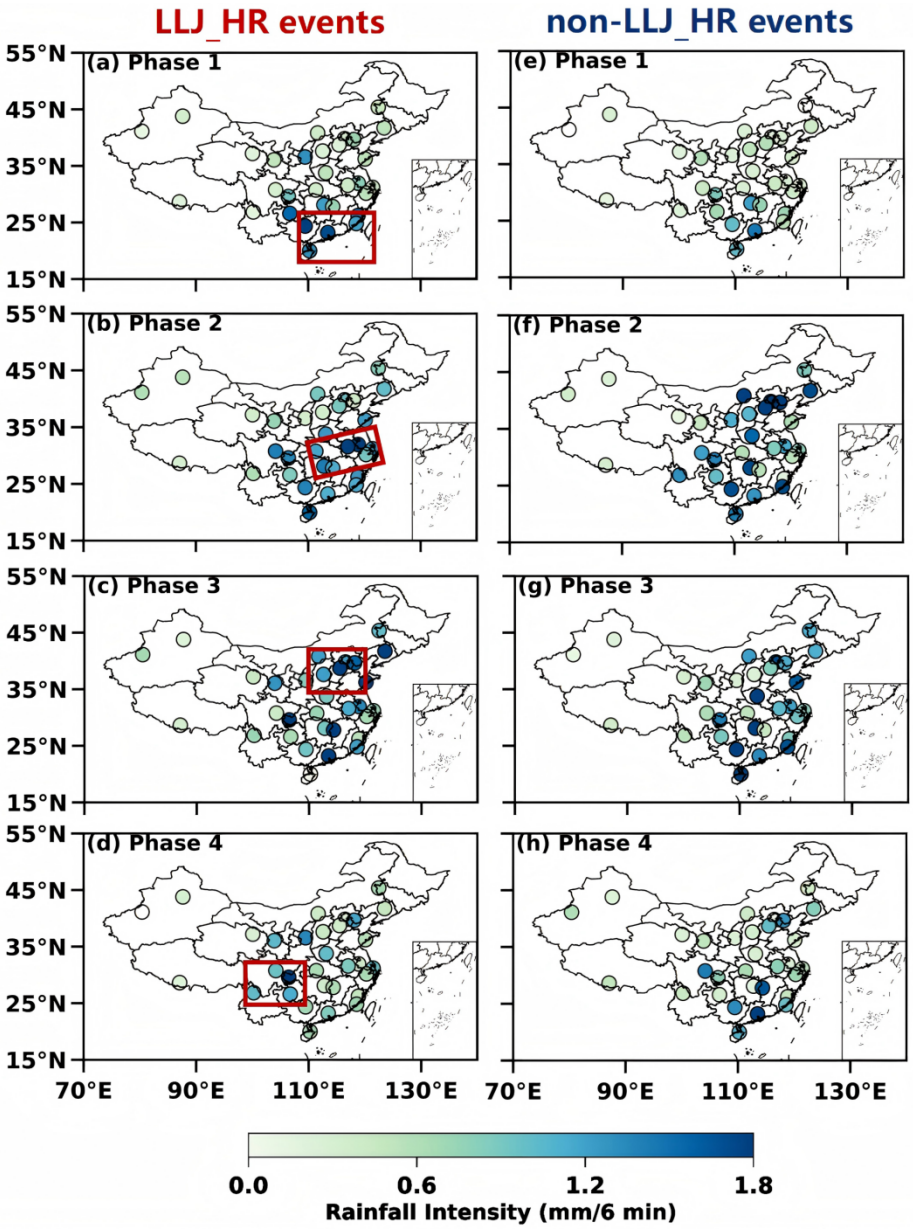

945

946 Figure 5. (a–d) Spatial distributions of site-averaged rain rate (mm/6 min) for nocturnal
947 LLJ_HR events during the warm season from Phase 1 to Phase 4 across China; (e–h)
948 Same as (a–d), but for non-LLJ_HR events. The red frame indicates four ROIs.

949

950

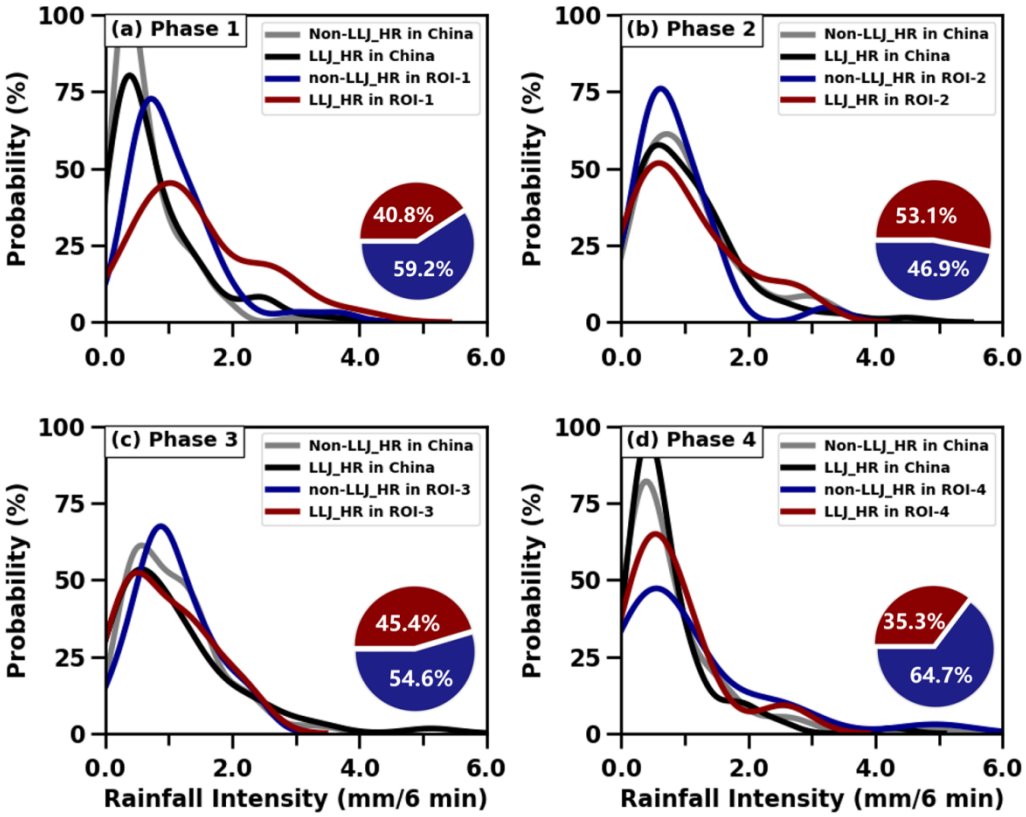

951

952 Figure 6. (a) Probability density distributions of average rain rate (mm/6 min) for
953 LLJ_HR events (black solid lines) and non-LLJ_HR events (gray solid lines) across
954 China during Phase 1, and specifically in ROI-1 for LLJ_HR events (red solid lines)
955 and non-LLJ_HR events (blue solid lines). (b-d) the same as panel (a), but for
956 comparisons between national-scale and other regional-scale events in ROI-2 during
957 Phase 2, ROI-3 during Phase 3, and ROI-4 during Phase 4. The pie chart at the lower
958 right shows the proportion distribution of LLJ_HR (red) and non-LLJ_HR (blue) events
959 in these key regions during each period

960

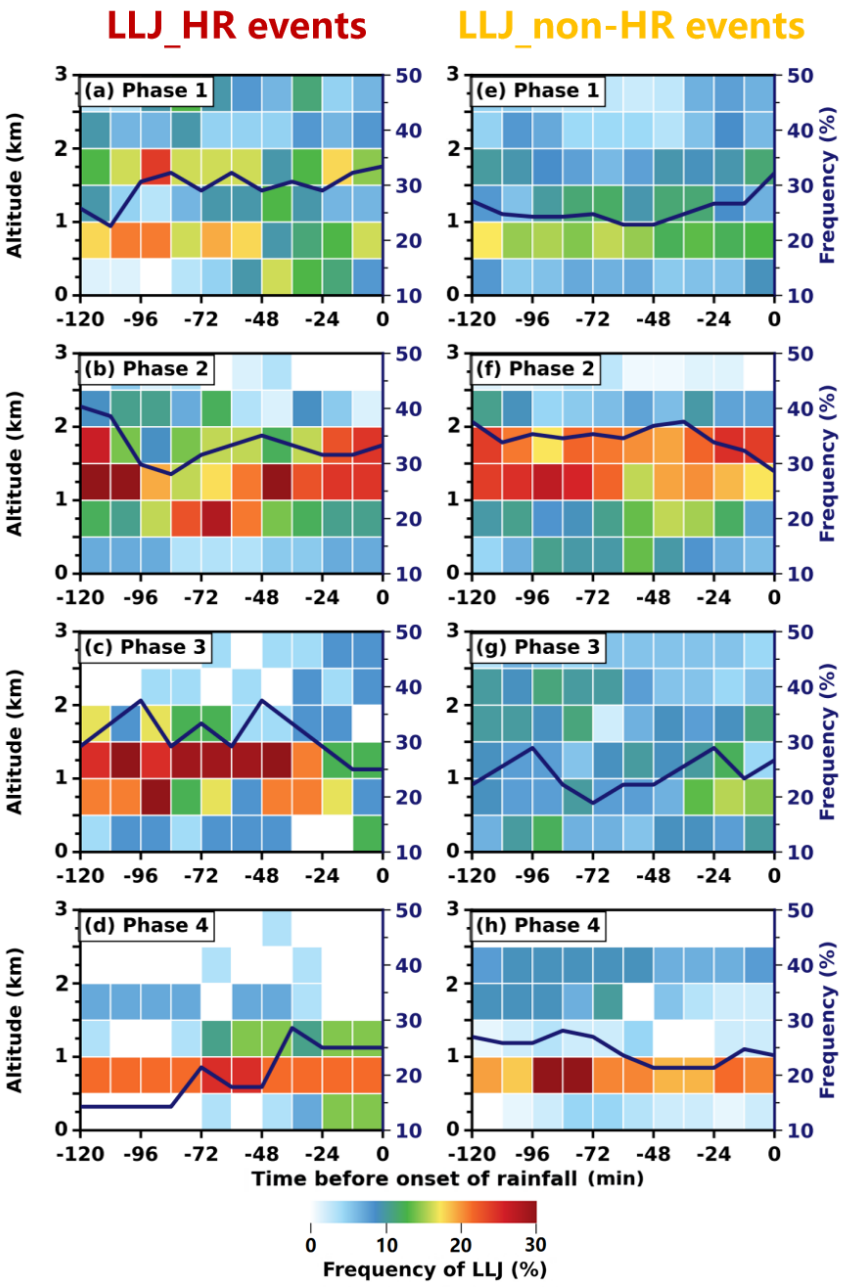

961

962 Figure 7. Time-height evolution of LLJ occurrence frequency (color shading, every 12
963 min, within 500 m vertical bins) detected by RWP with 2 hours preceding nocturnal
964 rainfall in LLJ_HR events in (a) ROI-1 during Phase 1, (b) ROI-2 during Phase 2, (c)
965 ROI-3 during Phase 3, and (d) in ROI-4 during Phase 4. Dark blue solid lines denote
966 accumulated LLJ frequency over 0–3 km latitude. (e-h) Same as (a-d), but for LLJ_non-
967 HR events

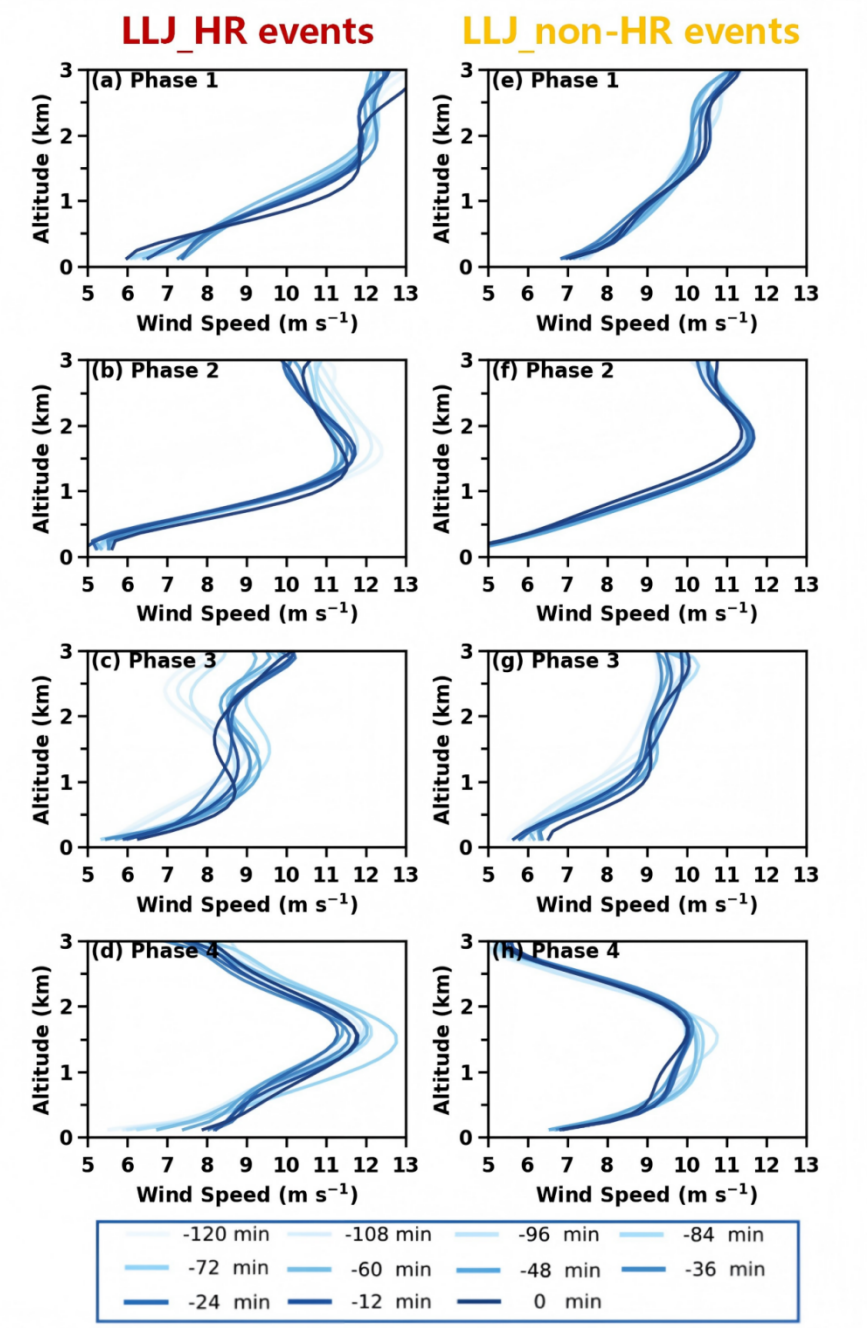

968

969 Figure 8. (a-d) Evolution of RWP-detected mean wind profiles of LLJs (blue solid lines,
970 every 12 min) within 2 hours preceding nocturnal rainfall in LLJ_HR events in (a) ROI-
971 1 during Phase 1, (b) ROI-2 during Phase 2, (c) ROI-3 during Phase 3, and (d) in ROI-
972 4 during Phase 4. (e-h) Same as (a-d), but for LLJ_non-HR events

973

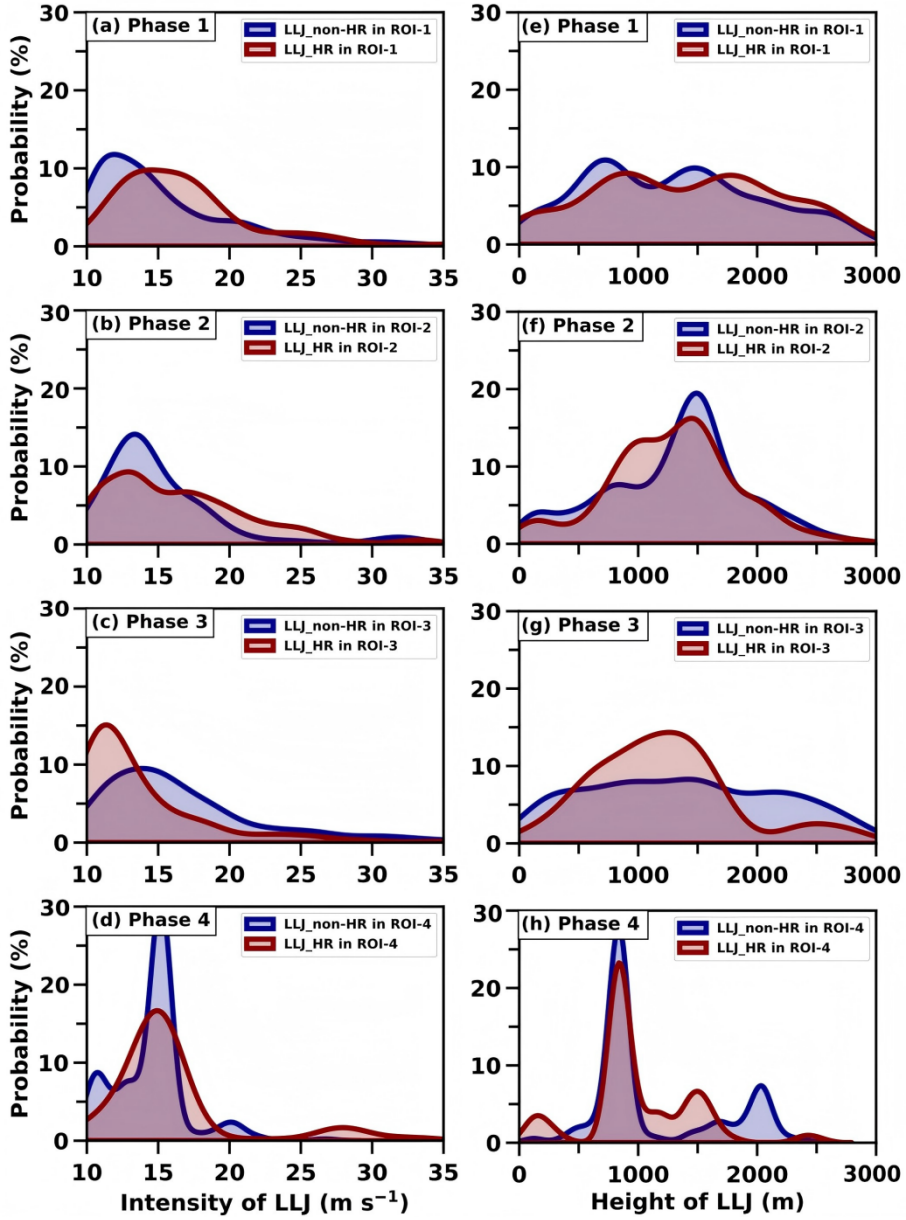

974

975 Figure 9. Probability density distributions of jet core intensity from RWP observations
976 within 2 hours preceding nocturnal rainfall in LLJ_HR events in (a) ROI-1 during Phase
977 1, (b) ROI-2 during Phase 2, (c) ROI-3 during Phase 3, and (d) in ROI-4 during Phase
978 4. (e-h) Same as (a-d), but for the height of LLJs

979

980

981

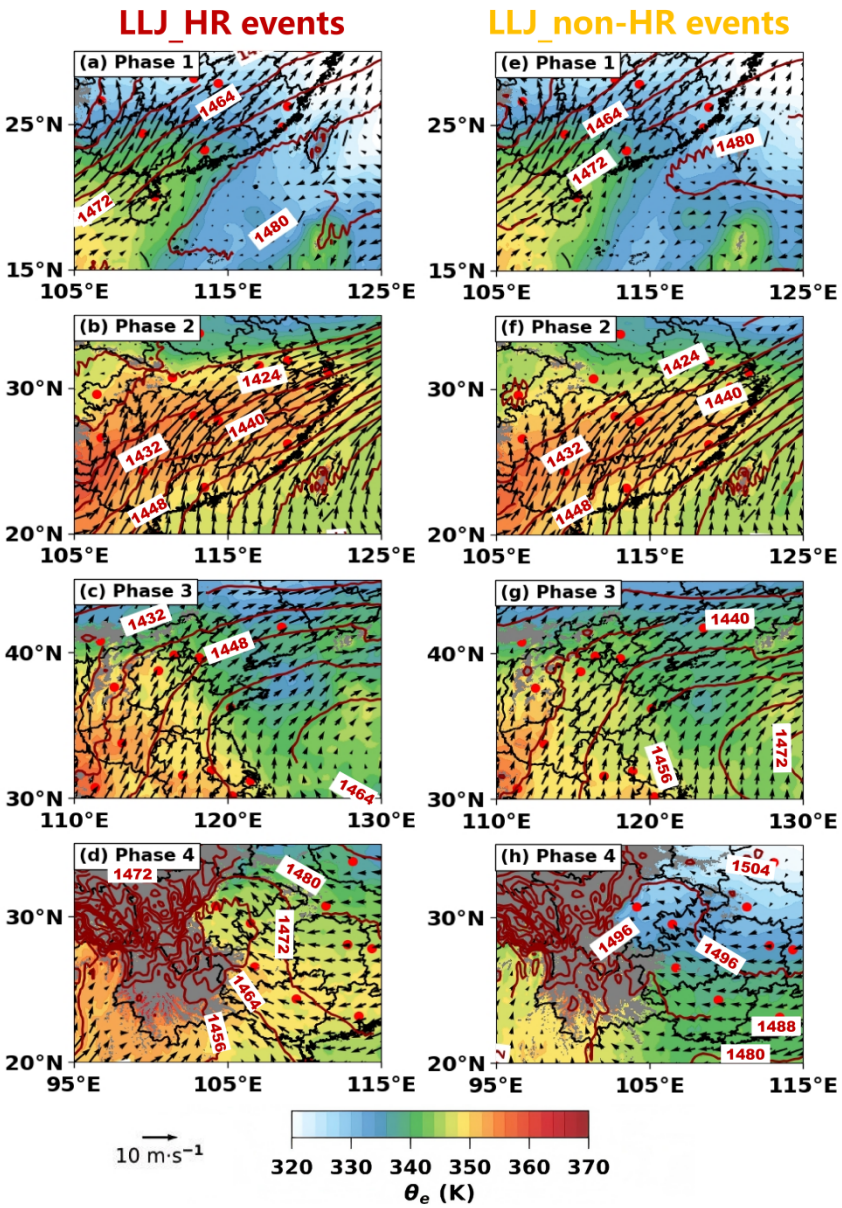

982

983 Figure 10. Distributions of equivalent potential temperature (shading, unit: K) at 850
984 hPa, superimposed with 850 hPa horizontal wind vectors (black arrows) and
985 geopotential height contours (red solid lines), for LLJ_HR events within 1-hour time
986 window preceding nocturnal rainfall onset in (a) ROI-1 during Phase 1, (b) ROI-2
987 during Phase 2, (c) ROI-3 during Phase 3, and (d) in ROI-4 during Phase 4. Gray
988 shading denotes terrain elevation exceeding 850 hPa level. The reference vector (10
989 m s^{-1}) is shown at the lower-left corner. (e-h) Same as (a-d), but for LLJ_non-HR events

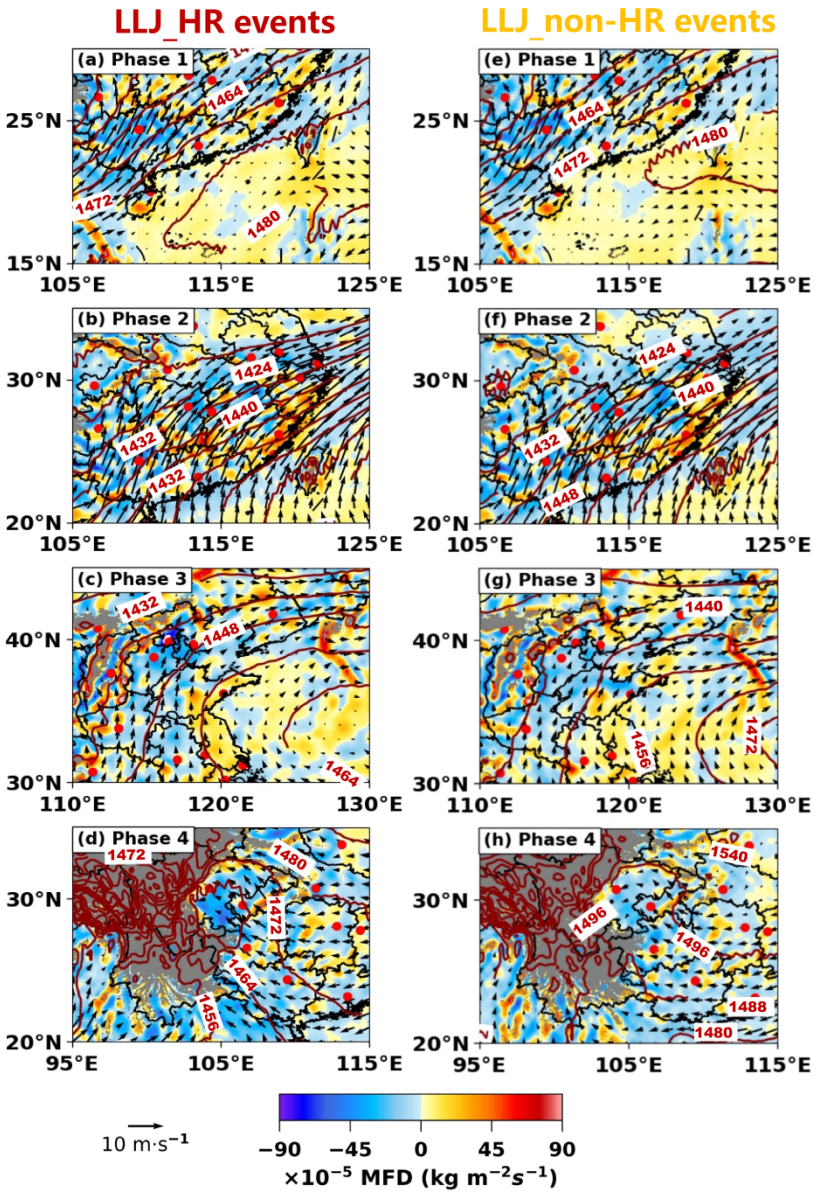

990

991 Figure 11. Same as Figure 10, but showing the integrated moisture flux divergence

992 (shading, unit: kg m^{-2} s^{-1}) between 1000–700 hPa at 1 hour prior to preceding

993 nocturnal rainfall onset

994

995

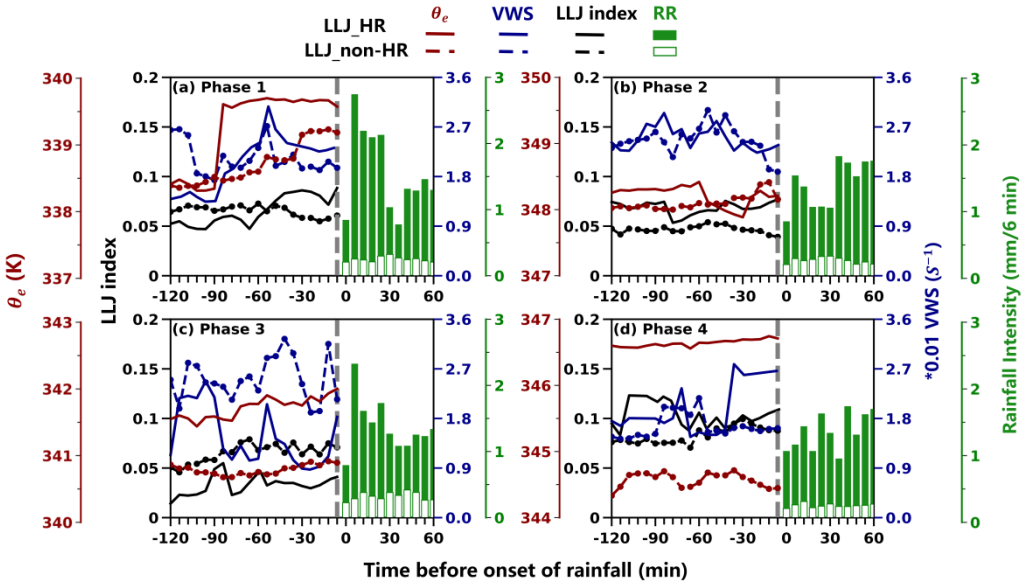

996

997 Figure 12. Temporal evolution of surface equivalent potential temperature (θ_e, red
998 lines), vertical wind shear (VWS, blue lines), and LLJ index (black lines) averaged
999 within 2 hours preceding nocturnal rainfall for LLJ_HR events (solid lines) and
1000 LLJ_non-HR events (dashed lines) in (a) ROI-1 during Phase 1, (b) ROI-2 during Phase
1001 2, (c) ROI-3 during Phase 3, and (d) in ROI-4 during Phase 4. Green bars denote 6-min
1002 averaged rain rate (mm/ 6 min) after LLJ_HR (solid bars) and LLJ_non-HR (open bars)
1003 events onset.